J Nanopart Res (2022) 24: 172
https://doi.org/10.1007/s11051-022-05545-w

RESEARCH PAPER

Photocatalytic degradation of tetracycline wastewater through heterojunction based on 2D rhombic $ZrMo_2O_8$ nanosheet and nano-TiO_2

**Chen Chen · Mingyue Wen · Ting Cheng ·
Lei Wang · Xiao Zhang · Yuan Tian**

Received: 5 March 2022 / Accepted: 28 July 2022 /

Abstract Herein, a novel composite heterojunction photocatalyst based on 2D rhombic $ZrMo_2O_8$ nanosheet and nano-TiO_2 was successfully constructed, synthesized, and characterized, and it demonstrated superior photocatalytic activity to degrade tetracycline wastewater. The composite photocatalyst exhibited prominent light absorption ability, remarkable stability, and recyclability, and the optimal ratio of Ti/Zr was 1/0.35. As proved by detection of DMPO-·OH, DMPO-O_2^-, and scavenging tests, the active species of ·OH and $·O_2^-$ played a major role in the degradation of tetracycline. The composite of TiO_2 and $ZrMo_2O_8$ could reduce the resistance of charge transfer and significantly decrease the recombination possibility of photo-induced electrons and holes. DFT calculation revealed that, when $ZrMo_2O_8$ (p-type semiconductor) and TiO_2 (n-type) meet with each other, electrons and holes would be transferred and achieved a unified Fermi level between them. Simultaneously, an internal electric field would be formed at the contact interface, and it promoted the transformation of electrons and prevented the propagation of holes in the same direction when excited by UV light. That achieved the effective separation of photo-generated electrons and holes and contributed to the excellent photocatalytic performance for degrading tetracycline. This work not only provides a new approach to construct the composite heterojunction photocatalyst, but also demonstrates the possibility of utilizing binary nanocomposites for enhanced photocatalytic degradation of antibiotic wastewater.

Keywords Photocatalyst · Heterojunction · $ZrMo_2O_8$ · TiO_2 · DFT calculation

Introduction

In modern society, with the great development of industrialization and urbanization, more and more wastewater is discharged into the environment [1]. Industries, such as textile [2], dyeing [3], electroplating [4], paper [5], food processing [6], and pharmaceutical [7], consume plenty of water resources for various production and discharge enormous wastes. Antibiotic-containing wastewater, like tetracycline (TC), ciprofloxacin (CIP), penicillin (PCN), oxytetracycline (OTC), and streptomycin (SM), is one of the most harmful types of industrial organic wastewater

---

C. Chen (✉) · M. Wen · L. Wang · Y. Tian
School of Environmental and Chemical Engineering,
Jiangsu University of Science and Technology,
Zhenjiang 212100, People's Republic of China
e-mail: chenc@just.edu.cn

T. Cheng · X. Zhang
School of Environmental Ecology, Jiangsu City Vocational
College, Nanjing 210017, People's Republic of China

X. Zhang
Nanjing University and Yancheng Academy
of Environmental Technology and Engineering,
Yancheng 224000, People's Republic of China

[8, 9]. Generally speaking, if this type of wastewater, containing complicated toxic and harmful organic substances, is discharged without proper treatment, it will pose a serious threat to the environmental safety and human health [10, 11]. Therefore, the treatment techniques of antibiotic wastewater have aroused considerable attention of many researchers in environmental field.

At present, the treatment techniques of antibiotic wastewater mainly include biological degradation [12], adsorption [13], chemical methods [14], membrane separation [15], advanced oxidation technologies [16], photocatalysis [17], and so on. As we know, each process has its own advantage and disadvantage. The biodegradation is relatively mature, but stringent reaction conditions and well-domesticated microorganisms are required. The equipment and operation of adsorption are simple, while the disposal of waste adsorbent (a hazardous waste) has become another problem. Chemical methods can achieve better treatment efficiencies, but the consumption cost is expensive. Membrane separation has good selectivity and low energy consumption, whereas it exists membrane contamination and regeneration problems. Advanced oxidation technologies, including traditional Fenton method, Fenton-like method, electrochemical oxidation, supercritical water oxidation, and wet air oxidation, are generally required higher treatment costs. Compared with these techniques above, photocatalysis is one of the most promising antibiotic wastewater treatment strategies owing to its high efficiencies, ambient operating conditions, being environment-friendly, recyclability, and low operating costs [18, 19].

Photocatalysis is one of ideal wastewater treatment processes developed in recent years, and it is reported to transfer the solar energy into the chemical energy with the help of photocatalyst [20]. Photocatalysis can be employed to achieve the degradation of environmental pollutants [21–23], the transformation of organic substances [24], the reduction of heavy metals [25] and CO_2 [26, 27], hydrogen production [28–30], overall water splitting [31], and so on. The main mechanism of photocatalysis is to use the photo-produced electrons (and derived oxygen radicals) and the photo-produced holes (and derived hydroxyl radicals) of semiconductor photocatalysts to degrade pollutants in the wastewater. Namely, electrons in semiconductor materials can transit from the valence band to conduction band and form photo-produced electrons in conduction band and photo-produced holes in valence band under the excitation of light. As one of crucial factors in photocatalysis, highly efficient photocatalysts play an important part to remove pollutants, thus attracting great efforts to develop. The traditional photocatalysts mainly include TiO_2 [32, 33], C_3N_4 [34–36], Ag_3PO_4 [37–39], ZnO [40, 41], ZrO_2 [42, 43], MoS_2 [44, 45], $ZnSnO_3$ [46], and they can accelerate the removal rates of pollutants to a certain degree. In addition to traditional catalysts, many new photocatalysts have been developed in recent years, and $Zr(MoO_4)_2$ is one of them [47–49].

In order to exploit the potential of photocatalysts as much as possible, the development of nanoscale photocatalysts has attracted the attention of many scholars. As a classical photocatalyst, TiO_2 has obtained many research results in the field of photocatalysis. Liu et al. [50] studied three types of nano-TiO_2 and pointed out that it can effectively photocatalytically degrade benzylamine. Lin et al. [51] applied nano-TiO_2 colloid to photocatalytic degradation of gaseous formalin and achieved gratifying results. Meanwhile, the synthesis of photocatalysts with special 2D structure was also one of the ways to effectively improve the photocatalytic performance. Moradi et al. anchored CuO nanoparticles and ZnO nanorods on g-C_3N_4 nanosheets. The compound material was applied to the photocatalytic decontamination of amoxicillin, and the results were satisfactory [52]. Liang et al. [53] suggested the Co-doped MoS_2 nanosheet could considerably improve the C_3N_4 photocatalytic hydrogen evolution activity as co-catalyst. As a photocatalytic material with a layered crystal structure, $Zr(MoO_4)_2$ also could theoretically obtain a special 2D nanosheet structure through rational synthesis method optimization, thereby improving its photocatalytic activity.

Moreover, the degradation effect of single photocatalysts is generally limited due to their restricted light absorption range and poor charge separation, generating negative impact to the recombination of photo-produced electron–hole pairs. This negative impact would hinder the improvement of photocatalytic efficiencies. Accordingly, efforts have been making to focus on a composite photocatalyst heterojunction, which would effectively reduce the recombination rate of photo-produced electron–hole pairs and expand the light absorption range [54]. You et al. [55] had prepared a CdS/C_3N_4 heterojunction that greatly promoted the photocatalytic degradation of rhodamine B. Su et al. [56] synthesized a bioinspired hierarchical $BiVO_4$/BiOCl heterojunction, proving its excellent photocatalytic degradation activity for the phenol. Zhang et al. [57] pointed out that the heterojunction photocatalyst gained from Ag_3PO_4 and $CdWO_4$ effectively promoted the photocatalytic degradation of rhodamine B. Combined the advantages of nanomaterials/2D materials with the photocatalyst heterojunction, the 2D rhombic $ZrMo_2O_8$ nanosheet in this work was firstly synthesized. Based on this, the photocatalyst heterostructure was successfully synthesized by compounding it with nano-TiO_2. The photocatalyst was characterized by many modern instruments, including X-ray diffraction (XRD), UV–vis diffuse reflectance spectra (UV–vis), scanning electron microscopy–energy-dispersive spectroscopy (SEM–EDX), X-ray photoelectron spectroscopy (XPS), transmission electron microscopy (TEM), and so on. Also, we utilized the tetracycline to verify the photocatalytic effect of composite materials. The impact factors, including photocatalyst types, reaction time, whether to provide the radiation of light, and the kinetics of photocatalytic reaction, were studied in experiments. Besides, the photocatalytic degradation performance, mineral phase, and the microscopic morphology of reused photocatalyst were evaluated. The solid photoluminescence (PL), the electron spin resonance (ESR), and the electrochemical analysis were also conducted to deeply illustrate the photocatalysis mechanism. Besides, the software of Vienna Ab initio Simulation Package (VASP) and the theory computation of spin-polarized density functional theory (DFT) were employed to reveal the transformation of photoinduced electrons and holes. The findings of experiments and theoretical calculation demonstrated that the composite catalyst (Ti@0.35Zr) exhibited outstanding photocatalytic activities to degrade the tetracycline. Moreover, these findings were highly recommended to develop more suitable photocatalysts to degrade antibiotics and alleviate the environmental pollution.

Experiments and methods

Synthesis of catalyst

The original nano-TiO_2 sample (hereinafter referred to as TiO_2) was bought from Sigma-Aldrich (USA). The synthesis method of original 2D rhombic $ZrMo_2O_8$ nanosheet (hereinafter referred to as $ZrMo_2O_8$) was as follows: First of all, 0.054 g of zirconium nitrate ($Zr(NO_3)_4{\cdot}5H_2O$) was dissolved into 100 mL of deionized water, and then treated by ultrasonic for about 30 min to obtain transparent solution. Secondly, 0.11 g of ammonium molybdate ($(NH_4)_2MoO_4$) was dissolved into 100 mL of deionized water (348 K) to obtain transparent solution. Thirdly, after the two solutions obtained in above steps were mixed, the mixture was transferred to three 100 mL of steel autoclaves with Teflon-lined stainless and reacted at 433 K for 10 h in a blast drying oven. After the reaction was completed, the mixture was cooled naturally, and the supernatant was poured out; then, the remaining white powder was put into the centrifuge tube and was centrifuged with deionized water and alcohol several times. And then, the centrifuged material was taken out after the water and product completely separated. The synthetic product was drying in a blast drying oven at 378 K to constant weight, and original 2D rhombic $ZrMo_2O_8$ nanosheet was acquired.

The synthesis method of a composite catalyst of $ZrMo_2O_8$ and TiO_2 was as follows: 0.054 g of zirconium nitrate ($Zr(NO_3)_4{\cdot}5H_2O$) and a certain amount of TiO_2 (the mole ratio of Ti and Zr ranged from 1/0.15 to 1/0.75) were dissolved into 100 mL of deionized water, and then treated by ultrasonic for about 45 min to obtain a homogeneous mixture. The subsequent synthesis steps were the same as those of original $ZrMo_2O_8$. The synthetic product was named as Ti@0.15Zr to Ti@0.75Zr.

Characterization of materials

To clarify various properties of fabricated materials, photocatalysts were characterized by many advanced equipment. The morphologies of materials were observed by the Hitachi S-3400 N scanning electron microscope and FEI Talos F200s transmission electron microscope, equipped with the high-angle annular dark-field scanning transmission electron microscopy (HAADF-STEM) and FEI Super-X EDS detector. The mineral composition of materials was measured by XRD patterns of the Shimadzu XD-3A diffractometer, employing the radiation of Cu-Kα ($\lambda = 1.54056$ Å). The surface chemical composition of catalysts was examined by PHI 5000 VersaProbe X-ray photoelectron spectroscopy spectra. The optical properties of materials were detected by UV–vis spectra using the PerkinElmer ultraviolet spectrophotometer. The charge carrier separation was measured via the solid photoluminescence under 400 nm, utilizing the Hitachi F-7000 fluorescence spectrometer. The active species in photocatalytic systems were analyzed by electron spin resonance using an electron paramagnetic resonance spectrometer (EMXmicro-6/1/P/L, Karlsruhe, Germany), and 5,5-dimethyl-1-pyrroline *N*-oxide (DMPO) was selected as a capturing agent to trap the free radicals of $\cdot O_2^-$ and ·OH. The electrochemical impedance spectroscopy and photocurrent were measured by CHI 660E electrochemical workstation. The three-electrode system was used in the electrochemical test. The sample electrode was the working electrode. The platinum sheet electrode was the counter electrode, and the saturated calomel electrode was the reference electrode. The 0.2 mol/L Na_2SO_4 solution was the electrochemical test electrolyte.

Photocatalytic experiments

In experiments, tetracycline was used as a pollutant to investigate the degradation effect of photocatalyst under the irradiation of UV light (30-W Hg lamp). The intensity of UV light was about 21.9 $\mu W/cm^2$ (at 420 nm) and 11.7 $\mu W/cm^2$ (at 365 nm), which was measured by ultraviolet irradiatometer (manufactured by Beijing Normal University). In each test, photocatalyst (0.010 g) was put into 30 mL of tetracycline solution to maintain the initial concentration of 40 mg/L. All photocatalytic experiments were conducted at room temperature (298 K, control by indoor air conditioner), and the reaction liquids were put into a transparent photocatalytic reaction vessel. The photocatalytic reaction time was from − 15 to 50 min, and the UV light was turned at 0 min. The reaction without light (− 15 to 0 min) promoted the nearly adsorption saturation between photocatalyst and tetracycline. After the photocatalytic degradation experiment, ultraviolet visible spectrophotometer was used to measure the remnant concentration of tetracycline at 360 nm [58, 59].

In our research, to illustrate the photocatalytic mechanism of this reaction, the active species produced in the photocatalytic reaction were analyzed, and different types of capturing agents were put into the mixtures to quench the reactive species. These scavengers included 0.037 g of EDTA-2Na, 0.0094 g of *tert*-butyl alcohol (TBA), 0.0108 g of 1,4-benzoquinone (BQ), and 0.0142 g of CCl_4. In addition, to evaluate the photocatalytic properties of recycled photocatalyst, the consecutive cycles were done to determine the photocatalytic efficiencies of tetracycline, and the photocatalyst was reused for four times. After each recycled cycle, a 0.45-μm filter membrane was used to filter the photocatalyst from the reaction liquid, and the recycled photocatalyst was then washed by deionized water for several times. After that, the recycled sample was dried to a constant weight at 348 K in a blast drying oven for the next usage.

DFT calculation

To explain the improvement of photocatalytic performance and special properties of composite material more deeply, the theoretical computation was introduced to analyze and simulate the structure of the crystal model of photocatalyst. VASP software [60] and spin-polarized DFT were carried out to investigate the mechanism of photocatalytic reaction process. The exchange–correlation potential was computed by Perdew–Burke–Ernzerhof (PBE) functional [61, 62] within the generalized gradient approximation (GGA) method [63, 64]. Also, the cutoff energy was 450 eV and the K-point grids of dimensions 5×5×5 were in the computed process. Figure 1 displays the theory structure and the surface model of TiO_2 and $ZrMo_2O_8$. We calculated the band structure and density of states using the crystal model of TiO_2 (Fig. 1a) and $ZrMo_2O_8$ (Fig. 1b). The work function was also computed through the surface model of model of TiO_2 (Fig. 1c) and $ZrMo_2O_8$ (Fig. 1d). First of all, both the atomic coordinates and cell parameters of TiO_2 and $ZrMo_2O_8$ were optimized during the process of calculation. Besides, the theoretical crystal structure of TiO_2 was a cell unit, including 4 Ti atoms and 8 O atoms. The theoretical crystal structure of $ZrMo_2O_8$ was a cell unit, including 6 Zr atoms, 12 Mo atoms, and 48 O atoms.

Results and discussions

XRD

To analyze the mineral structure composition of samples, the XRD patterns of original TiO_2, $ZrMo_2O_8$,

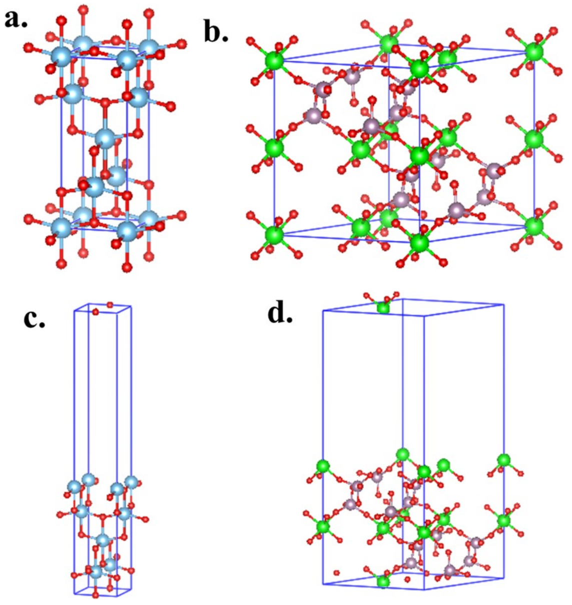

Fig. 1 The theory structure of the crystal model of TiO_2 (**a**) and $ZrMo_2O_8$ (**b**) and the theory structure of the surface model (for work function calculation) of TiO_2 (**c**) and $ZrMo_2O_8$ (**d**). The atom of O is red ball, the atom of Ti is blue gray ball, the atom of Zr is green ball, and the atom of Mo is grayish purple ball

and composite catalysts with different Ti/Zr ratios were measured, as shown in Fig. 2. It was observed that the main peaks of original TiO_2 could be found at 2θ: 25.28°, 27.36°, 37.78°, 48.00°, 53.94°, 55.06°, and 62.72°. The relative interplanar spacings were as follows: 0.352 nm, 0.326 nm, 0.238 nm, 0.189 nm, 0.170 nm, 0.169 nm, and 0.148 nm. These peaks were matched with the standard peaks of PDF#65–5714 (TiO_2). In addition, the characteristic diffraction peaks of original $ZrMo_2O_8$ were at 2θ: 18.16°, 21.62°, 24.78°, 27.30°, 30.00°, 30.99°, 34.22°, 35.94°, 41.88°, 47.50°, 51.06°, 51.34°, and 56.22°. The relative interplanar spacings were as follows: 0.488 nm, 0.411 nm, 0.359 nm, 0.326 nm, 0.298 nm, 0.288 nm, 0.262 nm, 0.250 nm, 0.215 nm, 0.191 nm, 0.179 nm, 0.178 nm, and 0.163 nm. Besides, for the composite catalysts, both the curves of TiO_2 and $ZrMo_2O_8$ could be clearly found in their XRD patterns. Also, with the growing of Ti ratio, the relative intensity of TiO_2 peaks increased gradually. Therefore, according to these analysis results of XRD, the composite photocatalysts should be the construction compounds of TiO_2 and $ZrMo_2O_8$.

Fig. 2 XRD patterns of original TiO_2, $ZrMo_2O_8$, and composite catalysts with different Ti/Zr ratios

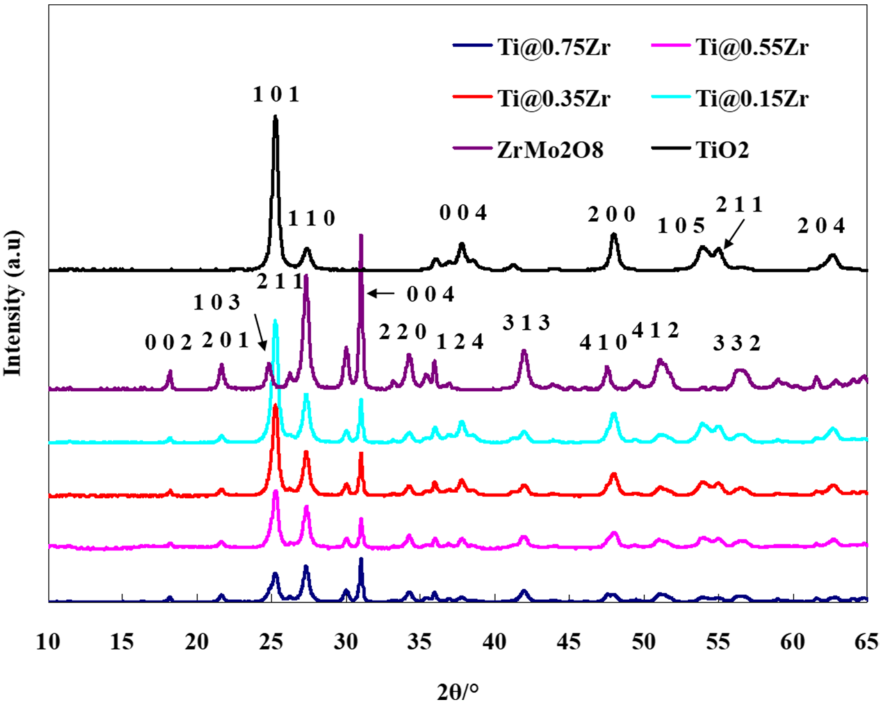

UV–vis diffuse reflectance spectra

The light absorption is one of the most crucial elements determining the performance of photocatalysis. UV–vis diffuse reflectance spectra were employed to evaluate the optical properties and the band gap of original TiO_2, $ZrMo_2O_8$, and composite catalysts with different Ti/Zr ratios, as depicted in Fig. 3. The absorption bands of $ZrMo_2O_8$ were around 250 to 400 nm. So, the $ZrMo_2O_8$ exhibited excellent absorption capacity for near-ultraviolet region light. As a recognized near-ultraviolet photocatalyst, the absorption bands of TiO_2 were around 250 to 415 nm. In addition, all the absorption bands of composite catalysts with different Ti/Zr ratios were between the original $ZrMo_2O_8$ and TiO_2. Besides, with the growing of Ti ratio, the absorption bands were gradually moved from $ZrMo_2O_8$ to TiO_2.

Tauc equation was employed to calculate the band gap energy of $ZrMo_2O_8$, TiO_2, and composite catalysts [65, 66]. The value of E_g can be obtained through plotting the curve of $[a(v)hv]^2$ versus hv and extrapolating the linear part of the curve to zero absorption coefficient. Herein, the band gap analysis and plotting process were conducted and are displayed in Fig. 3. The calculation results displayed that the band gap energy of original $ZrMo_2O_8$ and TiO_2 was 3.33 eV and 3.21 eV, respectively. Besides, the band gap calculation results of composite catalysts were between 3.33 and 3.21 eV, and the specific results were 3.31 eV (Ti@0.75Zr), 3.29 eV (Ti@0.55Zr), 3.27 eV (Ti@0.35Zr), and 3.25 eV (Ti@0.15Zr). Generally speaking, all these composite catalysts obtained excellent near-ultraviolet region light absorption abilities.

SEM–EDX

The SEM and EDX analytical technology was utilized to observe the microscopic morphology and composition of samples. Figure 4 depicts the SEM and EDX analytical results of $ZrMo_2O_8$. Obviously, the synthesized $ZrMo_2O_8$ presented the structure of a rhombic nanosheet. The side length of a rhombic nanosheet ranged from 400 to 600 nm, and the thickness of the nanosheet might be smaller than 20 nm. Also, Fig. 4c to f describes the element mapping area and analysis results. Elements of Mo, O, and Zr almost evenly distributed in the whole EDS analysis area, implying the sample should be $ZrMo_2O_8$. Figure 4h shows the element distribution results along the EDS line in Fig. 4c. All the elements including Mo, O, and Zr could be found along the EDS line, and the strength remained basically stable, which

Fig. 3 UV–vis diffuse reflectance spectra (plotting results of band gaps energy) for original TiO_2, $ZrMo_2O_8$, and composite catalysts with different Ti/Zr ratios

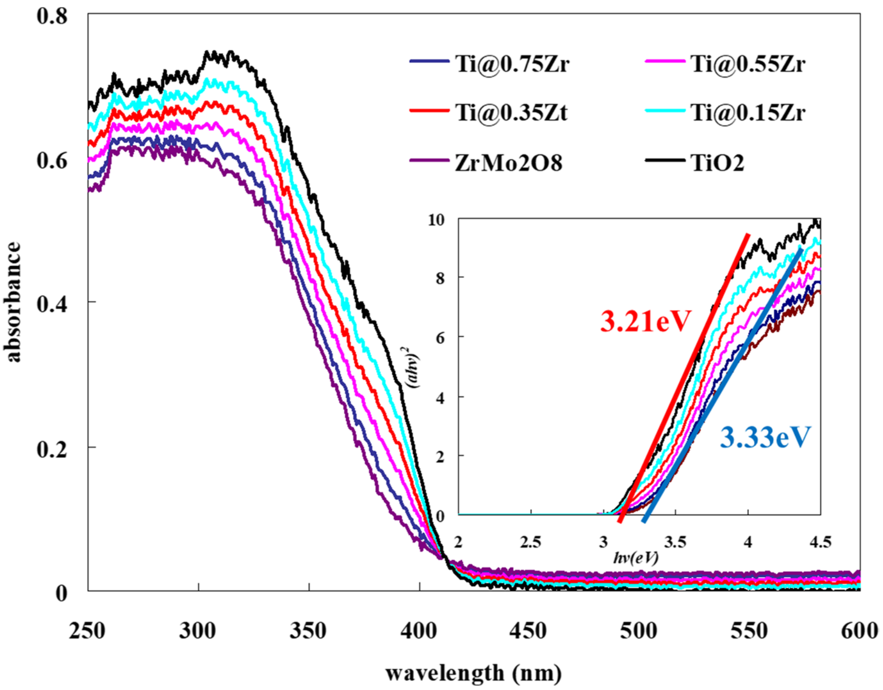

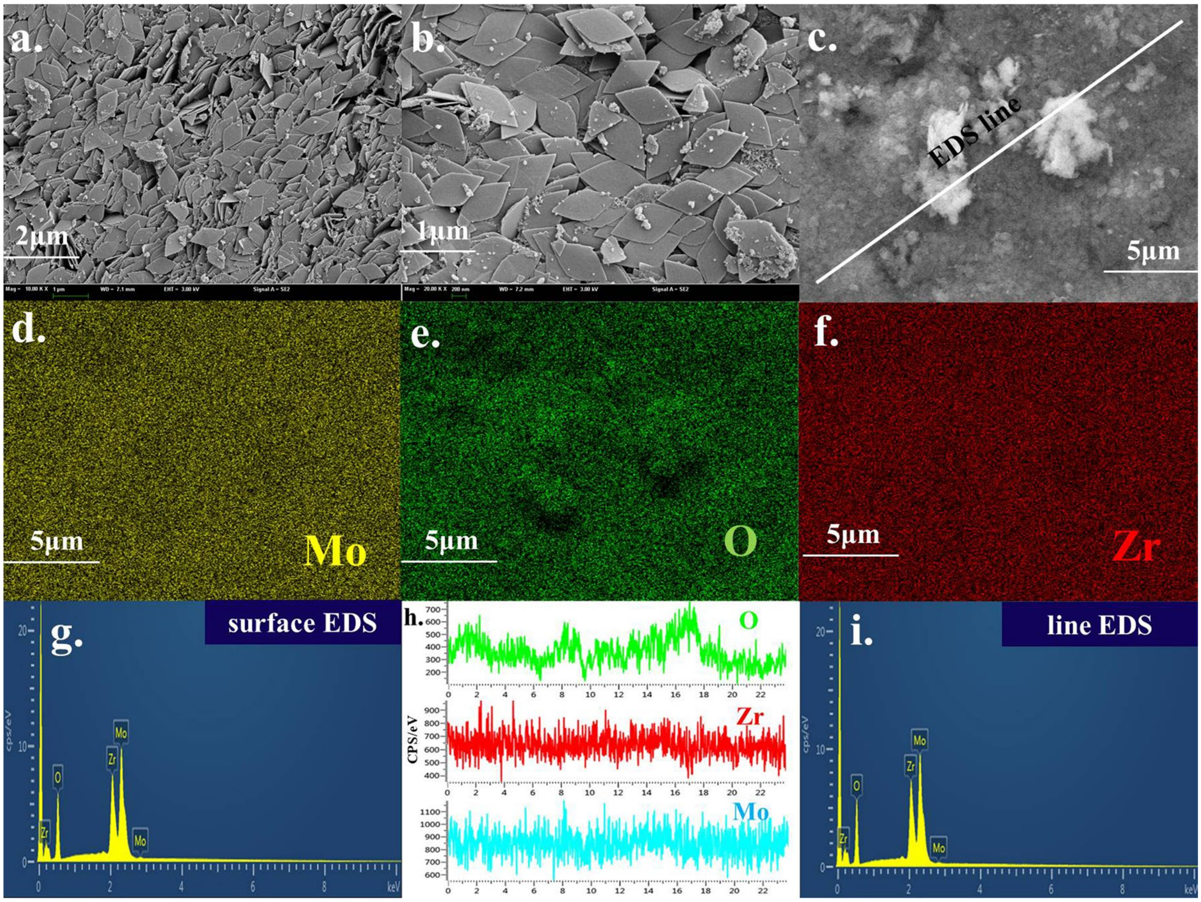

Fig. 4 SEM results of $ZrMo_2O_8$ nanosheet (**a** and **b**); EDS area and EDS line (**c**); EDS mapping results of Mo (**d**), O (**e**), and Zr (**f**); surface EDS results (**g**); element distribution results along the EDS line (**h**); and line EDS results (**i**)

further implied that the sample consisted of Mo, O, and Zr elements. Figure 4g and i shows the EDS area results of Fig. 4c and the total element composition results of the EDS line in Fig. 4c. The element compositions gained from Fig. 4g and i were basically the same as each other. The specific results (atom%) were as follows: Fig. 4g: 15.9% Mo, 9.74% Zr, and 74.36% O, and Fig. 4i: 16% Mo, 9.8% Zr, and 74.2% O. As a semi-quantitative analysis result, the element composition of EDS was basically in line with the molecular formula of $ZrMo_2O_8$. Consequently, the synthesized sample should be $ZrMo_2O_8$ nanosheet.

The morphology of a composite catalyst (Ti@0.35Zr) is depicted in Fig. 5a and b. As depicted in Fig. 5a, $ZrMo_2O_8$ nanosheet and nano-TiO_2 were tightly mixed together, and more details could be obtained from Fig. 5b. $ZrMo_2O_8$ still maintained the morphology of original rhombic nanosheet (the side length ranged from 400 to 600 nm, and the thickness was around 20 nm). Also, TiO_2 exhibited the morphology of nanoparticles, and the particle size ranged from about 20 to 40 nm. This closely combined heterojunction could be favorable to the transformation between photo-generated electrons and holes. Figure 5c to g shows the element mapping area and analysis results. The elements of Mo, O, Ti, and Zr were almost evenly distributed in the whole EDS analysis area, and that proved the composite was the homogeneous mixture of $ZrMo_2O_8$ and TiO_2. Figure 6c and f shows the element distribution results along the EDS line in Fig. 5c. It was presented that all the elements including Mo, O, Ti, and Zr could appear along the EDS line and the result strength

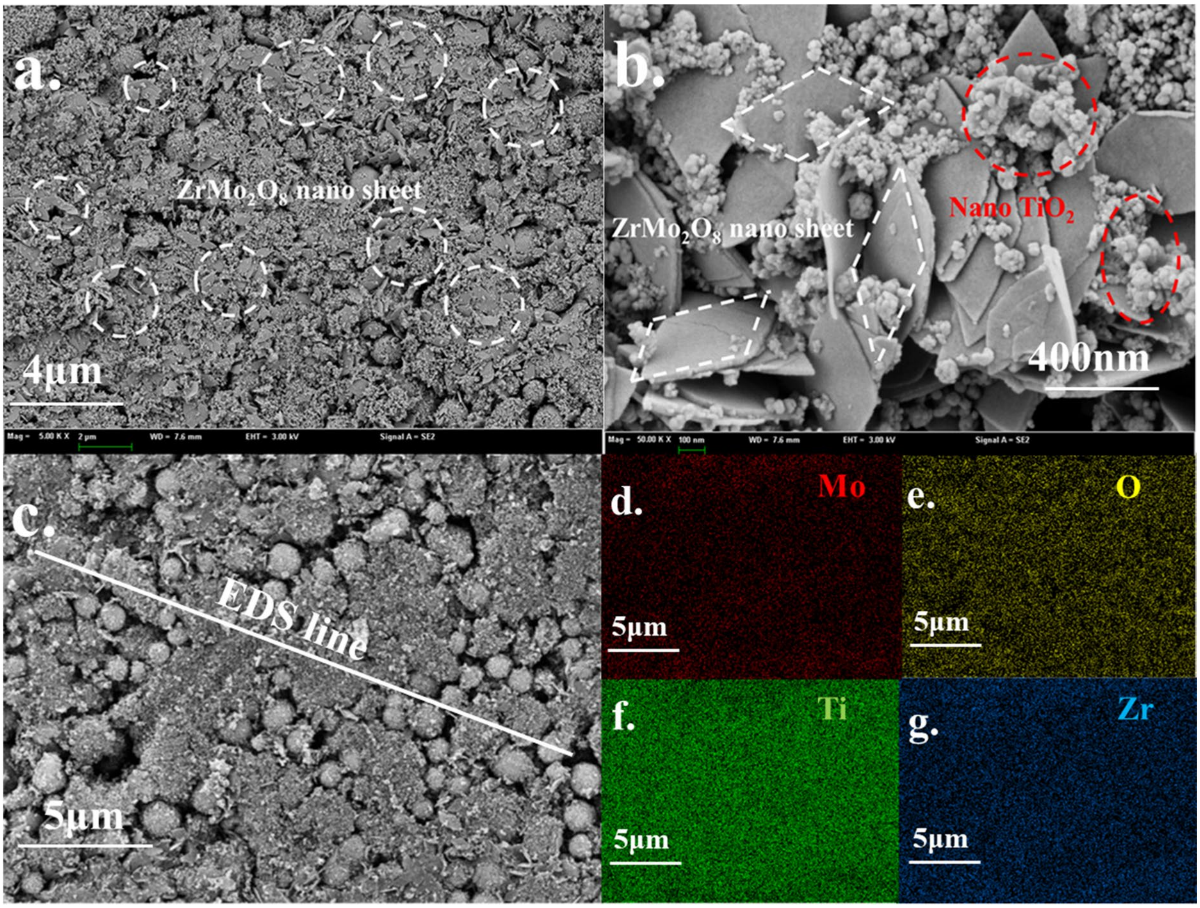

Fig. 5 SEM results of a composite catalyst (**a** and **b**, Ti@0.35Zr); EDS area and EDS line (**c**); and EDS mapping results of Mo (**d**), O (**e**), Ti (**f**), and Zr (**g**)

remained basically stable, which further stated the sample consisted of Mo, O, Ti, and Zr elements. Figure 6a and b depicts the EDS surface results and the total element composition results of the EDS line in Fig. 5c. The element compositions gained from Fig. 6a and b were basically the same as each other. The specific results (atom%) were as follows: Fig. 6a: 8.9% Mo, 5.4% Zr, 15.3% Ti, and 70.4% O, and Fig. 6b: 8.8% Mo, 5.2% Zr, 15.4% Ti, and 70.6% O. As a semi-quantitative analysis result, the element composition of EDS was mainly in agreement with the molecular formula of $ZrMo_2O_8$ and TiO_2. Therefore, the synthesized sample should be the heterojunction of $ZrMo_2O_8$ nanosheet and TiO_2 nanoparticles.

XPS

The XPS analysis of a composite catalyst (Ti@0.35Zr) was conducted to evaluate the surface chemical composition, as depicted in Fig. 7. The main curves of a composite catalyst (Ti@0.35Zr) appeared at around 564.1 eV (Ti2s), 530.1 eV (O1s), 464.1 eV and 459.1 eV (Ti2p), 416.1 eV and 398.1 eV (Mo3p), 336.1 eV and 333.1 eV (Zr3p), 233.2 eV (Mo3d), and 182.2 eV (Zr3d). All these curves belonged to elements of Zr, Mo, Ti, and O, which existed in the molecular formula of TiO_2 and $ZrMo_2O_8$. Also, we could obtain more information from the XPS spectra of high resolution of Mo3d, Zr3d, Ti2p, and O1s, as displayed in Fig. 7b to e.

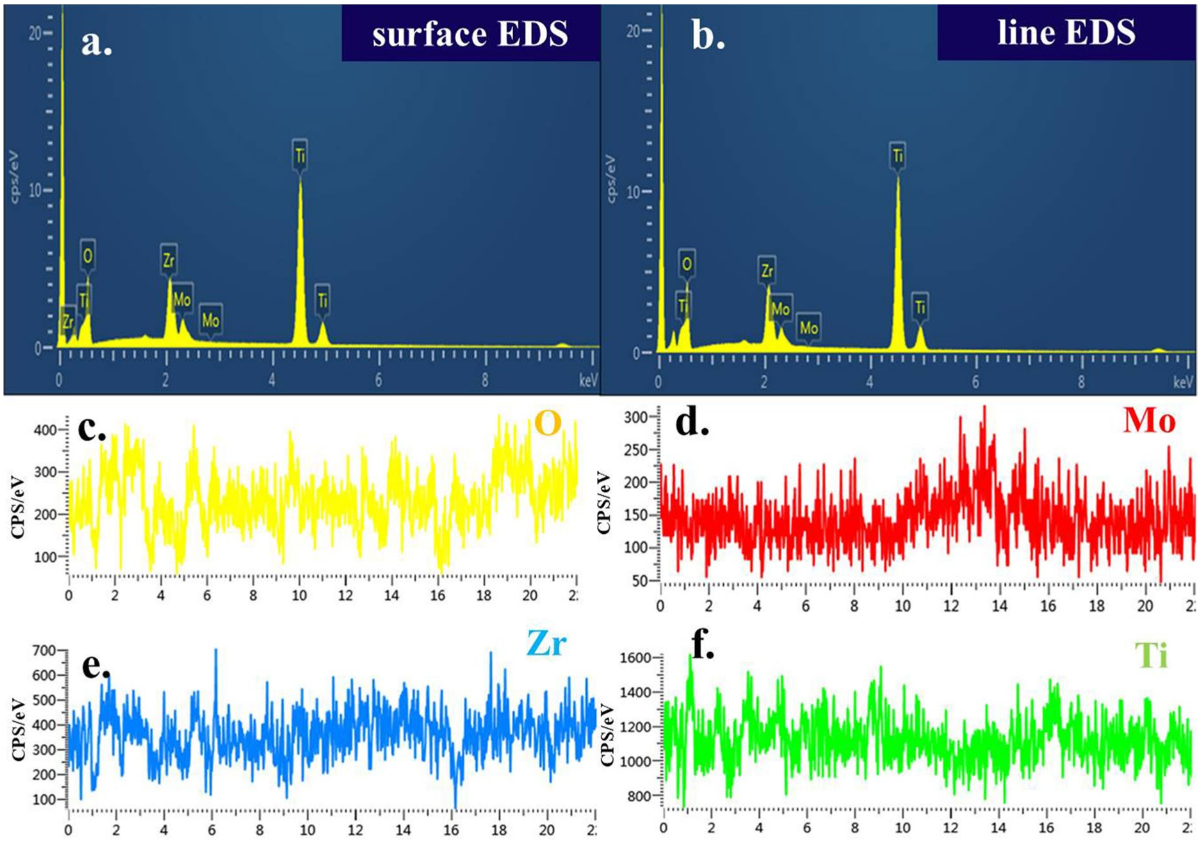

Fig. 6 The surface EDS results (**a**) and the line EDS results (**b**) in Fig. 5c of a composite catalyst (Ti@0.35Zr). Element distribution results along the EDS line (**c** to **f**) in Fig. 5c of a composite catalyst (Ti@0.35Zr)

The Mo3d$_{3/2}$ and Mo3d$_{5/2}$ spectra (in Fig. 7b) could be found at 235.7 eV and 232.5 eV, respectively. The appearance of Mo3d$_{3/2}$ and Mo3d$_{5/2}$ might be attributed to the Mo^{6+} in ZrMo$_2$O$_8$ [67]. Besides, it could be seen in Fig. 7c that Zr3d$_{3/2}$ and Zr3d$_{5/2}$ were found at 184.7 eV and 182.4 eV, respectively, which might be ascribed to the Zr^{4+} in ZrMo$_2$O$_8$ [68]. Moreover, Ti2p$_{3/2}$ and Ti2p$_{1/2}$ could be found at 458.4 eV and 463.9 eV in Fig. 7d, and that belonged to the Ti^{4+} in TiO$_2$ [22, 69]. Figure 7e displays the spectrum of O1s which could be split into peaks at 530.5 eV and 529.9 eV, and these two peaks might be corresponding to different O^{2-} in ZrMo$_2$O$_8$ and TiO$_2$, respectively. Additionally, the element proportion (atomic%) analysis results gained from XPS detection were 8.7% Mo, 4.4% Zr, 15.5% Ti, and 71.4% O, which were nearly consistent with the molecular formulas of ZrMo$_2$O$_8$ and TiO$_2$.

TEM

The TEM equipment with the high-angle annular dark-field scanning transmission electron microscopy was applied to further obtain the detail information of microscopic morphology and composition about composite photocatalyst, as displayed in Fig. 8 and Fig. 9. ZrMo$_2$O$_8$ nanosheets and TiO$_2$ nanoparticles were clearly observed in the composite catalyst (Ti@0.35Zr, Fig. 8a). Also, the side length of ZrMo$_2$O$_8$ nanosheets ranged from 400 to 600 nm, and the nanoparticle size of TiO$_2$ was around 20 to 50 nm. Meanwhile, it was presented that ZrMo$_2$O$_8$ and TiO$_2$ were closely combined to form a heterojunction. Figure 8c to g depicts the element mapping results of total elements (Mo, Zr, Ti, and O). Elements of Mo, Zr, and Ti were mainly distributed in the nanosheet region in Fig. 8a, while an element of O was relatively

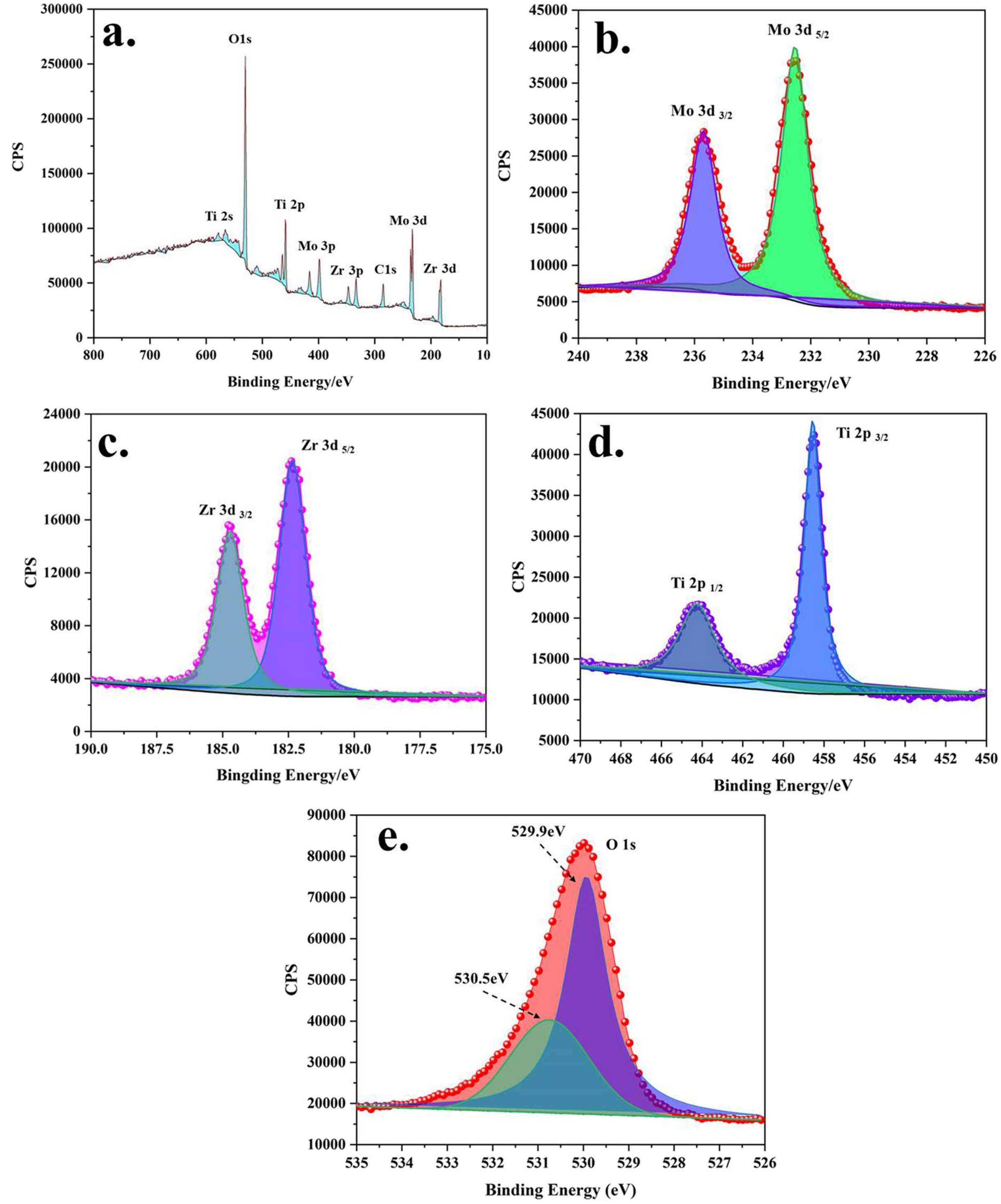

Fig. 7 **a** The wide-scan XPS of a composite catalyst (Ti@0.35Zr). The high-resolution XPS spectra of Mo3d (**b**), Zr3d (**c**), Ti2p (**d**), and O1s (**e**)

evenly scattered throughout the whole region, proving the existence of $ZrMo_2O_8$ nanosheets and TiO_2 nanoparticles once again. In addition, it was depicted in Fig. 8c to f that the element distribution of Mo, Zr, and Ti overlapped in some areas, indicating $ZrMo_2O_8$ nanosheet– and TiO_2 nanoparticle–constituted heterojunctions. Figure 8h depicts the element distribution results along the green line in Fig. 8c. The elements of Ti and O were mainly distributed during the line range of 0 to 380 nm, suggesting this area was mainly the nanoparticles of TiO_2.

Figure 9a further presents the TEM results of a composite catalyst (Ti@0.35Zr), and the rhombic $ZrMo_2O_8$ nanosheets and TiO_2 nanoparticles could be found. Figure 9b depicts the electron diffraction ring results. The diffraction rings (inside/1-out/8) represented 0.488 nm ($ZrMo_2O_8$), 0.352 nm (TiO_2), 0.288 nm ($ZrMo_2O_8$), 0.238 nm (TiO_2), 0.215 nm ($ZrMo_2O_8$), 0.189 nm (TiO_2), 0.169 nm (TiO_2), and 0.148 nm (TiO_2), respectively. Figure 9c to d shows the HRTEM images of composite catalysts. Combined with the results of XRD in Fig. 2, the 0.488-nm interplanar spacing (in Fig. 9d) and the 0.353-nm interplanar spacing (in Fig. 9c and e) might belong to $ZrMo_2O_8$ and TiO_2. This finding stated again that the rhombic nanosheets were $ZrMo_2O_8$ and the nanoparticles were TiO_2, and further proved the composite catalyst was the heterojunction of $ZrMo_2O_8$ and TiO_2.

The photocatalytic activities for tetracycline degradation

The photocatalytic activities of photocatalysts were investigated via tetracycline degradation experiments under light, as displayed in Fig. 10. The light was turn on at 0 min. Compared with the other four systems (pure TiO_2, pure $ZrMo_2O_8$, pure light, and Ti@0.35Zr without light), it was observed from Fig. 10a that systems of composite catalysts displayed higher photocatalytic efficiencies for the degradation of tetracycline. Figure 10a also stated that the composite catalyst of the Ti@0.35Zr system exhibited the best photocatalytic performance for tetracycline degradation in the presence of light. Moreover, changes of UV absorption spectra for tetracycline at the composite catalyst of Ti@0.35Zr photocatalytic system are displayed in Fig. 10d. It was seen that peaks of tetracycline were decreased gradually with the reaction time, which proved that tetracycline exhibited prominent photocatalytic activities in the composite catalyst of Ti@0.35Zr photocatalytic system.

In addition, the apparent degradation kinetics was investigated through the first-order reaction model [35, 66]. Based on the experimental data in Fig. 10a, the fitting results of apparent kinetics are depicted in Fig. 10b and Table 1. Except for Ti@0.35Zr without light system, the R^2 values of tetracycline degradation processes under the other seven systems were all above 0.97, indicating the photodegradation reaction of tetracycline in these seven systems could be suitably described through the first-order reaction model. The k values of degradation kinetics are shown in Fig. 10c and Table 1, and it was observed that the photocatalytic degradation system of Ti@0.35Zr exhibited the most ideal photodegradation activities.

Also, to evaluate the stability and recyclability of a composite catalyst (Ti@0.35Zr), the microscopic morphology and XRD patterns of reused material after four times of usage were analyzed, as presented in Fig. 11a and b. The initial microscopic morphology of the photocatalyst was basically maintained. After four times of consecutive photocatalytic tests (Fig. 11a), there was just a little variation in the appearance of photocatalyst (Ti@0.35Zr). In addition, from XRD patterns, after the 4th photocatalysis experiment (Fig. 11b), it was found that the main curves of TiO_2 and $ZrMo_2O_8$ could also appear in contrast with the previous results. At the same time, according to the reused photodegradation curves (Fig. 11c), there was only a slight reduction of photocatalytic activities after 4 cycles of recycle. These findings proved that the composite catalyst (Ti@0.35Zr) possessed remarkable photocatalytic stability, and the photocatalyst could be efficiently reused.

Photocatalytic degradation mechanism

The transient photocurrent responses of TiO_2, $ZrMo_2O_8$, and composite catalyst (Ti@0.35Zr) under the irradiation of Hg lamp are described in Fig. 12a. Single TiO_2 and $ZrMo_2O_8$ appeared to have a certain response, implying they were able to form many electrons and holes under the condition of UV light. Also, it was observed that the photocurrent intensity of a composite catalyst (Ti@0.35Zr) greatly improved, confirming that the composite material obtained stronger reflecting ability for the UV light. The

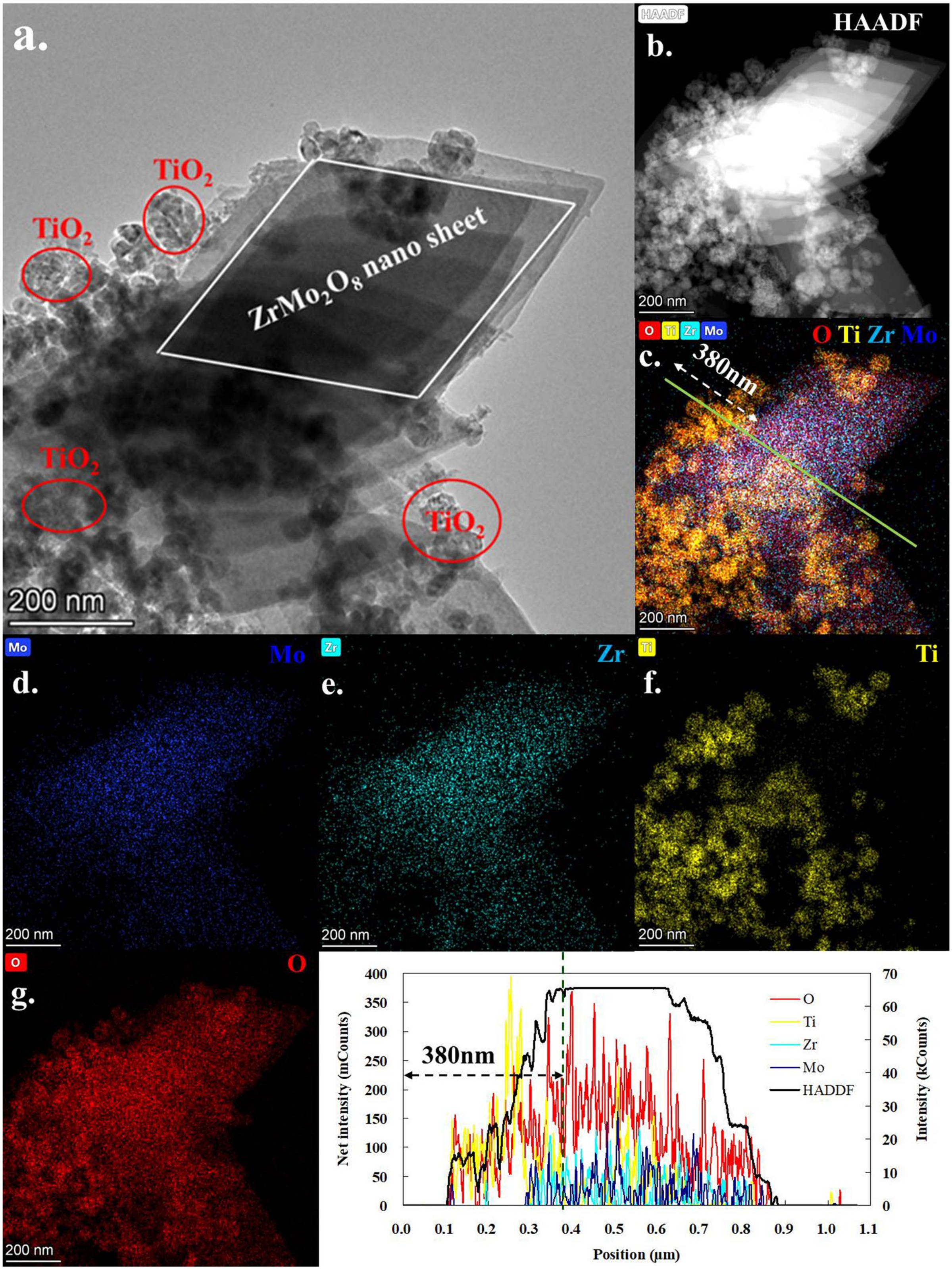
a.
TiO$_2$
TiO$_2$
ZrMo$_2$O$_8$ nano sheet
TiO$_2$
TiO$_2$
200 nm
HAADF
b.
HAADF
200 nm
O Ti Zr Mo
c.
O Ti Zr Mo
380nm
200 nm
Mo
d.
Mo
200 nm
Zr
e.
Zr
200 nm
Ti
f.
Ti
200 nm
O
g.
O
200 nm
380nm
Net intensity (mCounts)
Intensity (kCounts)
Position (µm)
0
50
100
150
200
250
300
350
400
0
10
20
30
40
50
60
70
0.0
0.1
0.2
0.3
0.4
0.5
0.6
0.7
0.8
0.9
1.0
1.1
O
Ti
Zr
Mo
HADDF

◂**Fig. 8** **a**, **b** TEM and HAADF results of a composite catalyst (Ti@0.35Zr); element mapping results of total elements (**c**), Mo (**d**), Zr (**e**), Ti (**f**), and O (**g**); and **h** element distribution results along a line in **c**

highest photocurrent intensity also implied that the binary composite (TiO_2 and $ZrMo_2O_8$) was favorable to the generation and transfer of photo-produced electrons and photo-produced holes. The EIS values of TiO_2, $ZrMo_2O_8$, and composite catalyst (Ti@0.35Zr) are depicted in Fig. 12b. Among them, the radius values of a composite catalyst were the smallest, stating the composite of TiO_2 and $ZrMo_2O_8$ could reduce the resistance of charge transfer and hence effectively promoted the reaction process of photocatalysis [70]. Additionally, the PL emission spectrum was conducted to study the combination and separation possibility of photo-generated electrons and photo-generated holes, as shown as Fig. 12c. It was found that the photoluminescence spectrum intensity of TiO_2 was much higher than that of the other two photocatalysts. This finding indicated that the photo-induced electrons and holes produced by TiO_2 had the greatest recombination possibility. Besides, the lower photoluminescence spectrum intensity of $ZrMo_2O_8$ stated that the recombination possibility of electron and hole was lower than that of TiO_2. And then, the composite catalyst (Ti@0.35Zr) displayed the lowest photoluminescence spectrum intensity, suggesting the composite of TiO_2 and $ZrMo_2O_8$ could further contribute to the decrease of combination probability [71].

To verify the active species in the photocatalytic degradation process and clarify the action mechanism, the hydroxyl radicals (DMPO-·OH) and the superoxide radicals (DMPO-O_2^-) were measured using the DMPO technique by ESR spin-trapping spectra, as depicted in Fig. 13. There was no typical curves of ·OH or·O_2^- in the composite catalyst (Ti@0.35Zr) system without UV light, implying there were no electrons and holes excited in the absence of UV light. In contrast, both typical curves of ·OH with the intensity ratio of 1:2:2:1 and that of ·O_2^- were detected under the irradiation of UV light, proving the active radicals of ·OH and ·O_2^- were produced in the process of photodegradation. Hence, the action process of these free reactive radicals might be one of main photocatalytic mechanisms for the degradation of tetracycline. At the same time, the signal of ·OH in Fig. 13a was obviously stronger than that of ·O_2^- in Fig. 13b, indicating ·OH played a stronger role than that of ·O_2^- in the photocatalytic reaction process. Moreover, to further verify which species play active roles during the course of photocatalytic degradation, the capturing agents were put into the mixtures to capture the active species. On the basis of literatures, EDTA-2Na, TBA, BQ, and CCl_4 could be employed as hole, hydroxyl radical, oxygen, and electron trapper, respectively [21, 72]. Figure 13c presents the impact of different types of capturing agents on the photocatalytic efficiencies of tetracycline. After adding the capturing agents, the degradation efficiencies of tetracycline in all photocatalytic systems decreased, which proved the coexistence of scavengers could inhibit the photocatalytic activities of photocatalyst. Also, the degradation path of photocatalysis from Eqs. (1) and (4) might happen during the photodegradation process. Besides, it was presented that both EDTA-2Na and TBA displayed more significant impacts on the photodegradation reaction than the other two capturers. These findings implied the capturing of photo-produced holes and hydroxyl radicals probably lowers the photocatalytic activities of reaction process, and that was in line with ESR analytical results. The reaction (Eqs. (3) and (4)) by composite catalyst (Ti@0.35Zr) might be the main degradable pathway for tetracycline photodegradation.

$$O_2 + e^- \rightarrow \cdot O_2^- \tag{1}$$

$$\cdot O_2^-/e^- + \text{tetracycline} \rightarrow \text{degradation} - \text{products} \tag{2}$$

$$H_2O/OH^- + h^+ \rightarrow \cdot OH \tag{3}$$

$$\cdot OH/h^+ + \text{tetracycline} \rightarrow \text{degradation} - \text{products} \tag{4}$$

The DFT computation results of energy bands and density of states for TiO_2 are depicted in Fig. 14a and c. It was presented that the band gap value of TiO_2 was 1.96 eV. Meanwhile, from the energy band structure and DOS results of TiO_2, it appeared that the Fermi energy levels were approximated to the conduction band bottom, indicating TiO_2 was an n-type semiconductor material, theoretically. In addition, the DFT calculation of energy bands and density of states for $ZrMo_2O_8$ was also conducted. As depicted

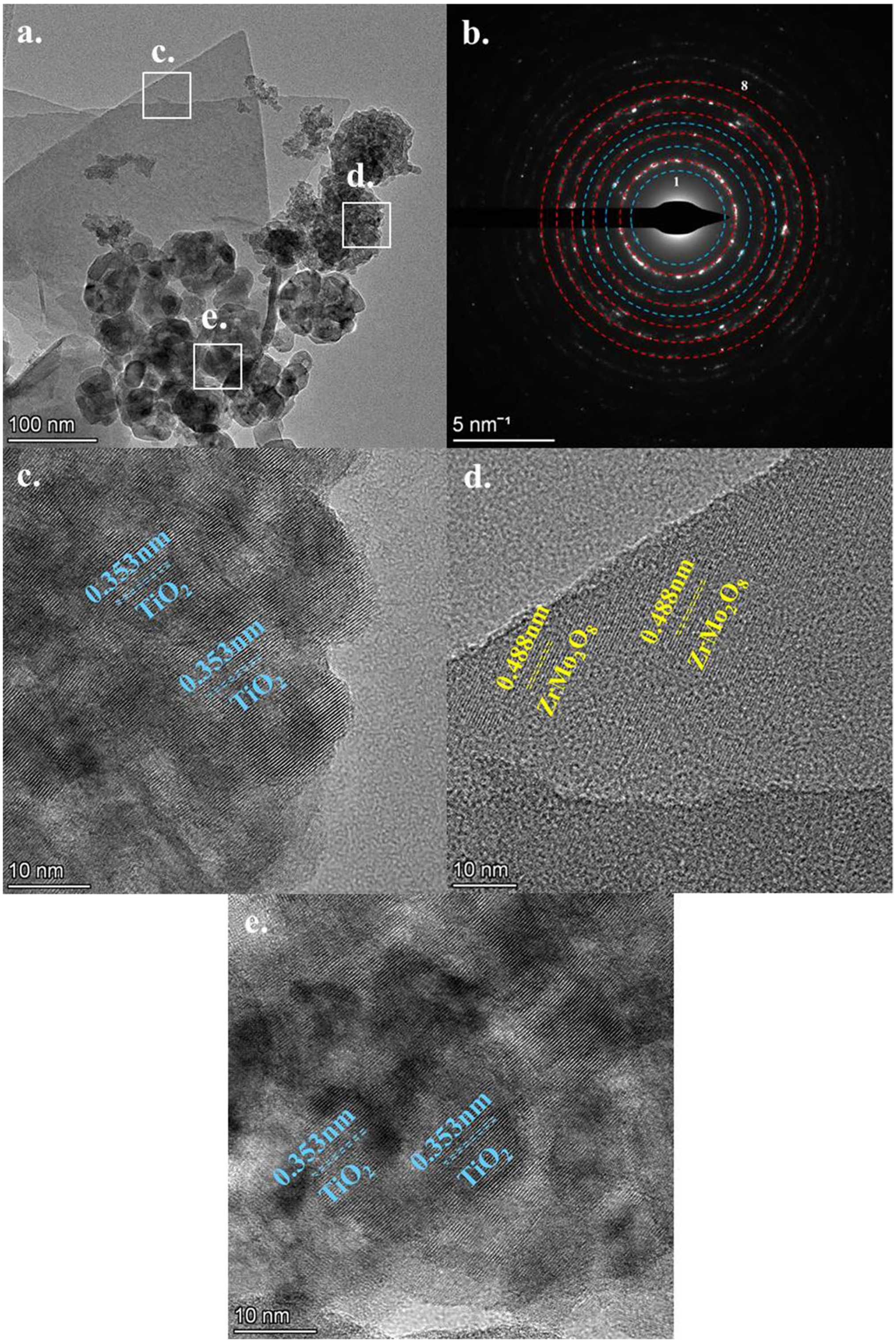

Fig. 9 TEM result (**a**) and HRTEM images (**b**–**d**) of a composite catalyst (Ti@0.35Zr) and TEM diffraction ring (**e**)

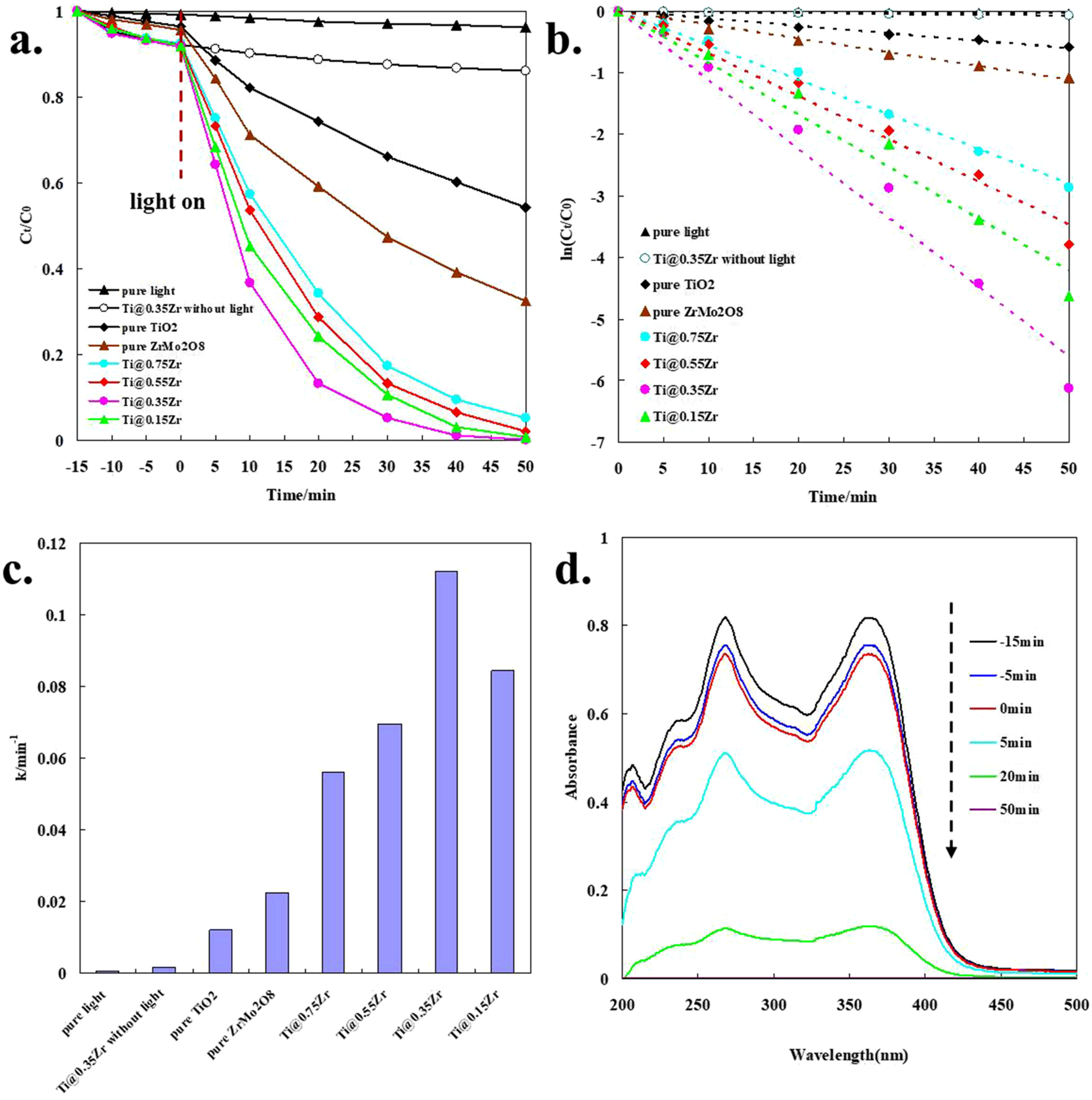

Fig. 10 **a** The comparison of different degradation reaction systems. **b** The fitting results of first-order reaction kinetics for photodegradation of tetracycline. **c** The constants in first-order reaction kinetics. **d** The absorption spectra of UV–visible for tetracycline solution degraded under the Ti@0.35Zr system

in Fig. 14b and d, the band gap value of $ZrMo_2O_8$ was 2.97 eV. Meanwhile, it was presented from the energy band structure and DOS results of $ZrMo_2O_8$ that the Fermi energy levels were approximated to the top of valence bands, implying $ZrMo_2O_8$ was a p-type semiconductor material in theory. Furthermore, both the band gap values of TiO_2 and $ZrMo_2O_8$ were smaller than the experimental values in some degree, and the explanation was generally ascribed to inherent defects of DFT calculation method. Moreover, the work function of TiO_2 and $ZrMo_2O_8$ is displayed in Fig. 15 through the DFT calculation. It was presented that the work function of TiO_2 and $ZrMo_2O_8$ was 4.3 eV and 5.50 eV, respectively.

Table 1 The-first-order rate constants calculated from the experimental data

Degradation reaction systems	Tetracycline	
	k (min^{-1})	R^2
Pure light	0.000629	0.9774
Ti@0.35Zr without light	0.00153	0.9394
Pure TiO_2	0.01198	0.986
Pure $ZrMo_2O_8$	0.0224	0.991
Ti@0.75Zr	0.0561	0.9954
Ti@0.55Zr	0.0694	0.9812
Ti@0.35Zr	0.112	0.977
Ti@0.15Zr	0.08448	0.9736

It is reported that when p-type and n-type semiconductors meet with each other, electrons would be transferred from materials with higher Fermi levels (TiO_2) to that of lower ones ($ZrMo_2O_8$), and holes would be moved in the opposite direction to electrons (Fig. 16a). Such movement of electrons and holes would eventually achieve a unified Fermi level between material of TiO_2 and $ZrMo_2O_8$. Simultaneously, an internal electric field (the direction was from TiO_2 to $ZrMo_2O_8$) would be formed at the contact interface between TiO_2 and $ZrMo_2O_8$. In this situation, when both TiO_2 and $ZrMo_2O_8$ were excited by UV light to produce photo-induced electrons and holes, the internal electric field would promote the

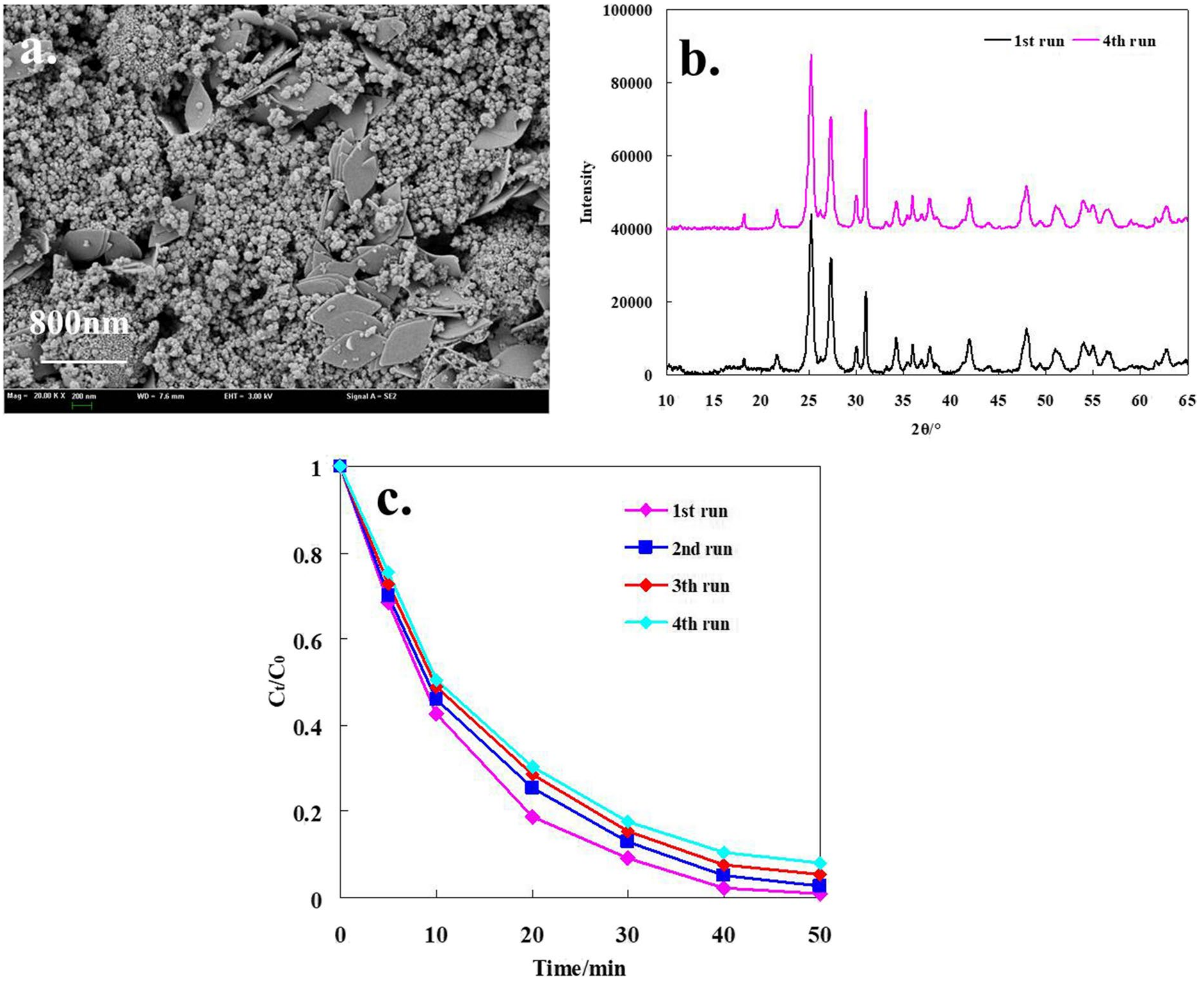

Fig. 11 **a** The morphology of a composite catalyst (Ti@0.35Zr) after the 4th photodegradation experiments. **b** The XRD patterns of a composite catalyst (Ti@0.35Zr) before and after the 4th photodegradation experiments. **c** The degradation curves of a composite catalyst (Ti@0.35Zr) reused under UV light

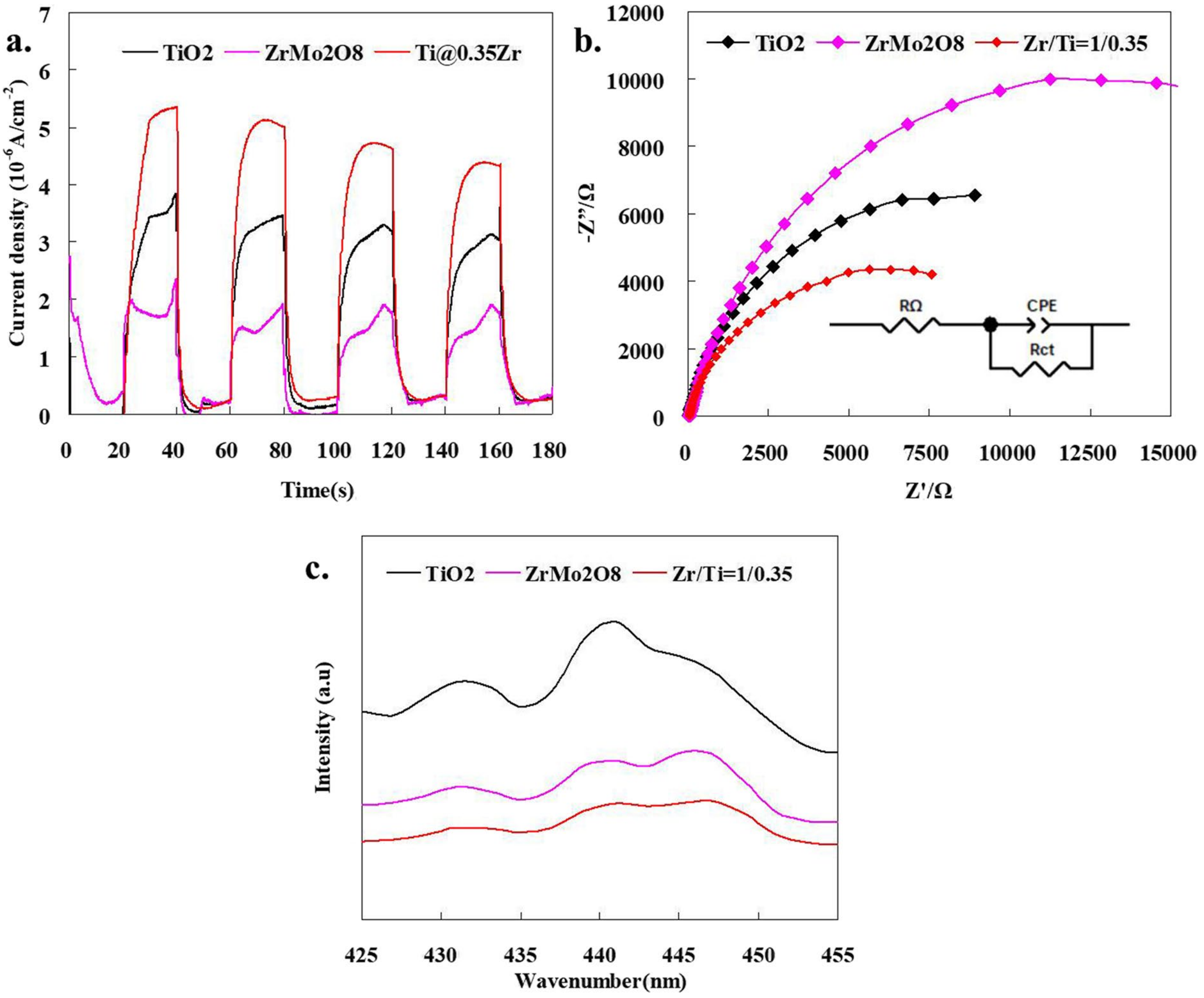

Fig. 12 Transient photocurrent responses (**a**), electrochemical impedance spectra (**b**), and steady-state PL spectra (**c**) of TiO_2, $ZrMo_2O_8$, and composite catalyst (Ti@0.35Zr)

transformation of electrons from $ZrMo_2O_8$ to TiO_2 and prevent the propagation of holes in the same direction (Fig. 16b). Similarly, the internal electric field would accelerate the transformation of holes from TiO_2 to $ZrMo_2O_8$ and inhibit the transfer of electrons in the same direction (Fig. 16b). Finally, such transformation process would promote the effective separation of photo-induced electrons and holes between TiO_2 and $ZrMo_2O_8$ and greatly improve the photocatalytic efficiencies of pollutant by the heterojunction composite of TiO_2 and $ZrMo_2O_8$. The schematic diagram of photocatalytic mechanism in the whole reaction process is described in Fig. 17.

Conclusions

In summary, a composite heterojunction photocatalyst was successfully synthesized by 2D rhombic $ZrMo_2O_8$ nanosheet and nano-TiO_2. The photocatalyst was characterized by XRD, UV-DRS, SEM–EDS, XPS, and TEM to verify various properties and was applied to photocatalytically degrade tetracycline under UV light. The composite photocatalysts displayed prominent light absorption ability, and the optimum composite ratio of Ti/Zr was 1/0.35. The composite catalyst effectively enhanced the photodegradation efficiencies of antibiotics and

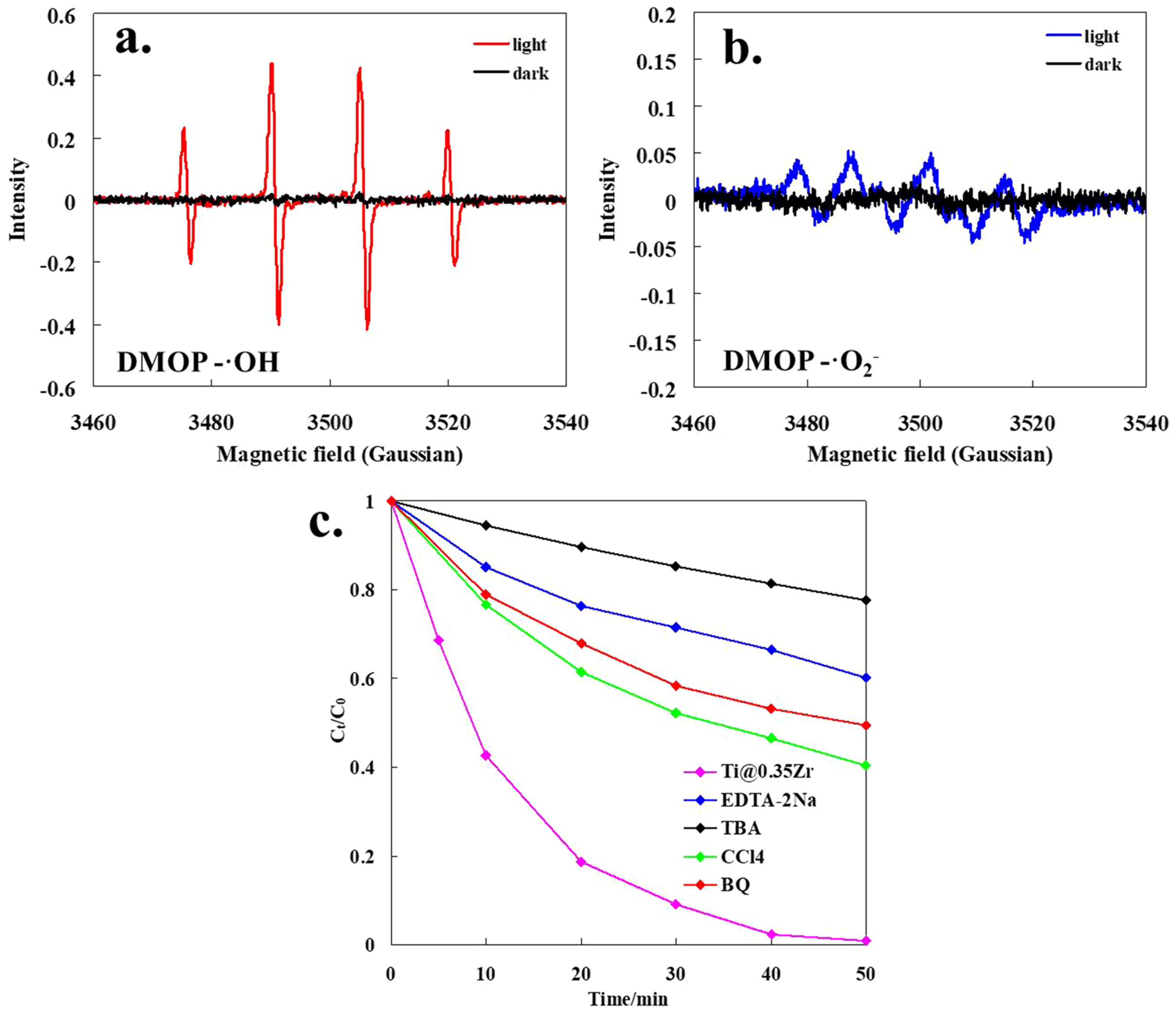

Fig. 13 **a** ESR spectra of radical adducts trapped by DMPO in the dark and under the irradiation of UV light for DMPO-·OH. **b** ESR spectra of radical adducts trapped by DMPO in the dark and under the irradiation of UV light for DMPO-·O_2^-. **c** The tetracycline photocatalytic efficiencies after the addition of capturing agents

exhibited excellent stability after 4 cycles of reuse. Besides, the active species of ·OH and ·O_2^- in the photocatalytic system were detected and played a major part in the degradation of tetracycline. The photocatalytic mechanism and DFT calculation findings illustrated that the composite heterojunction photocatalyst greatly reduced the recombination possibility of photo-induced electrons and holes and achieved the effective separation of photogenerated electrons and holes. When excited by UV light, the internal electric field formed by TiO_2 and $ZrMo_2O_8$ would promote the transformation of electrons from $ZrMo_2O_8$ to TiO_2 and prevent the propagation of holes in the same direction. Consequently, the photocatalytic degradation efficiencies of tetracycline were greatly improved. This work may provide new approaches to construct more suitable and effective photocatalysts to alleviate the pollution of antibiotic wastewater.

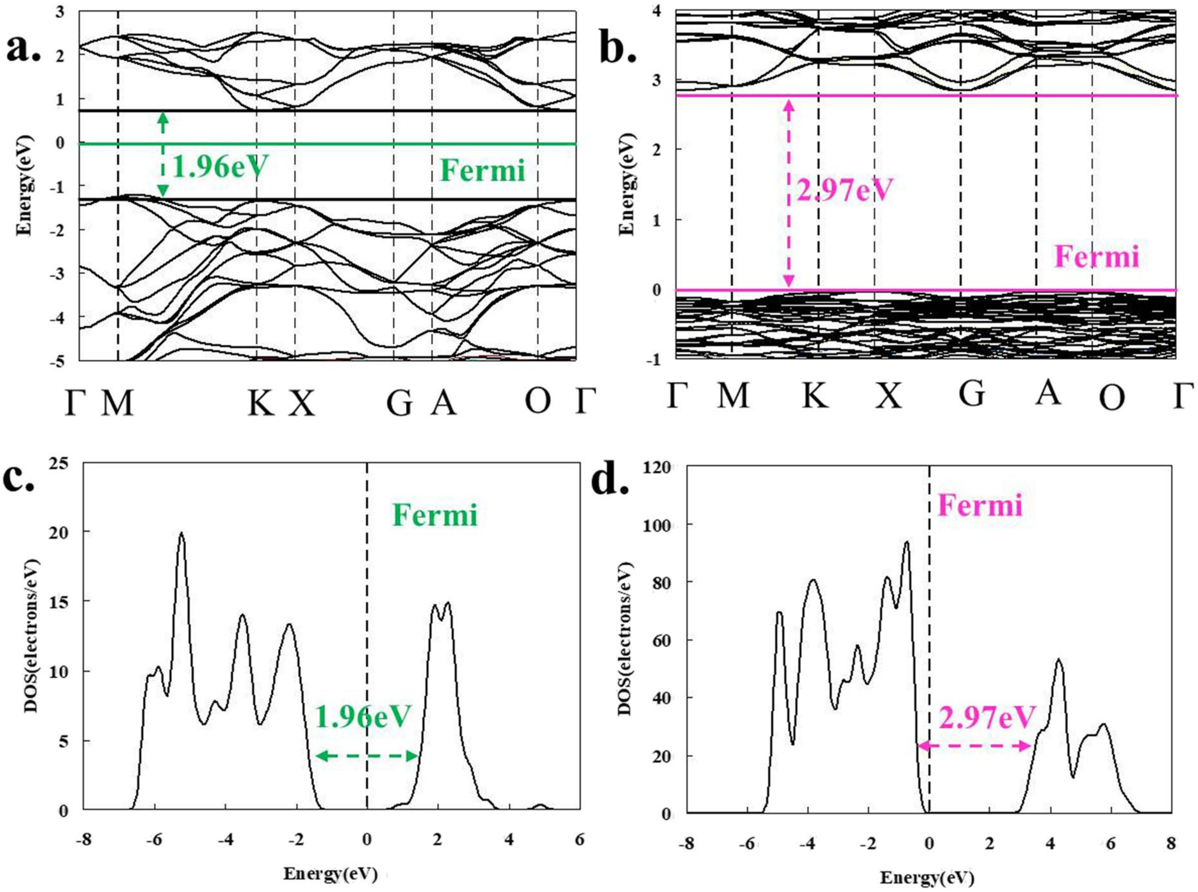

Fig. 14 Band structure and density of states of TiO_2 (**a** and **c**) and $ZrMo_2O_8$ (**b** and **d**) from DFT calculation

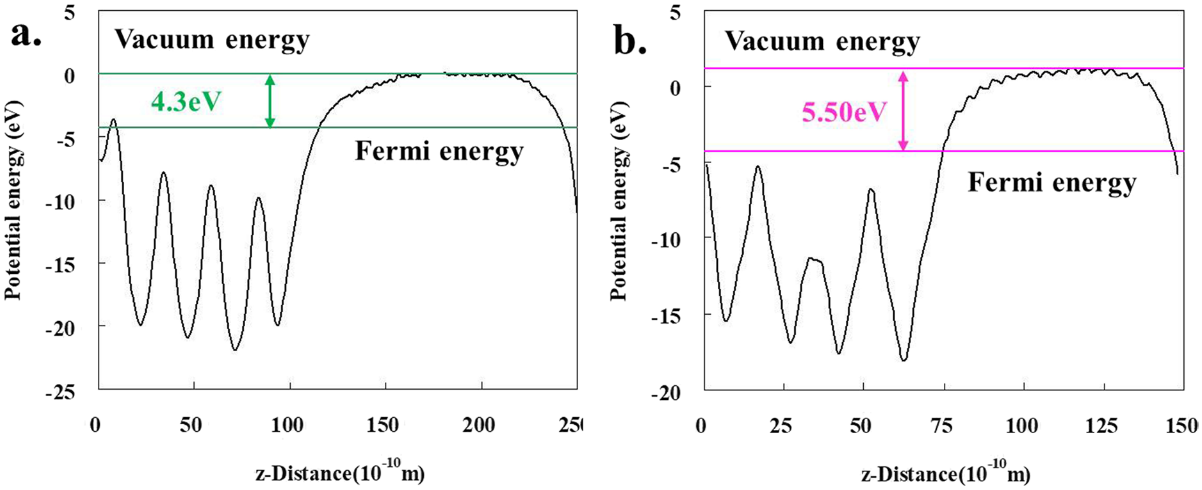

Fig. 15 The work function of TiO_2 (**a**) and $ZrMo_2O_8$ (**b**) from DFT calculation

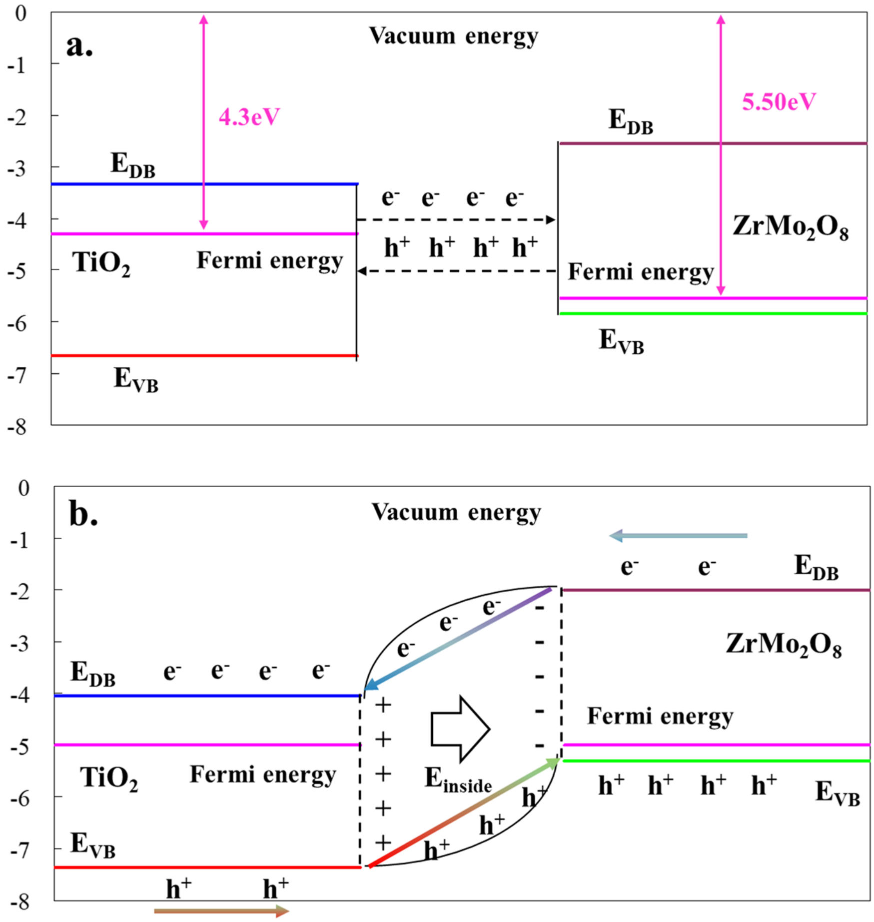

Fig. 16 **a** The formation process of internal electric field. **b** The electron and hole transfer process between TiO_2 and $ZrMo_2O_8$

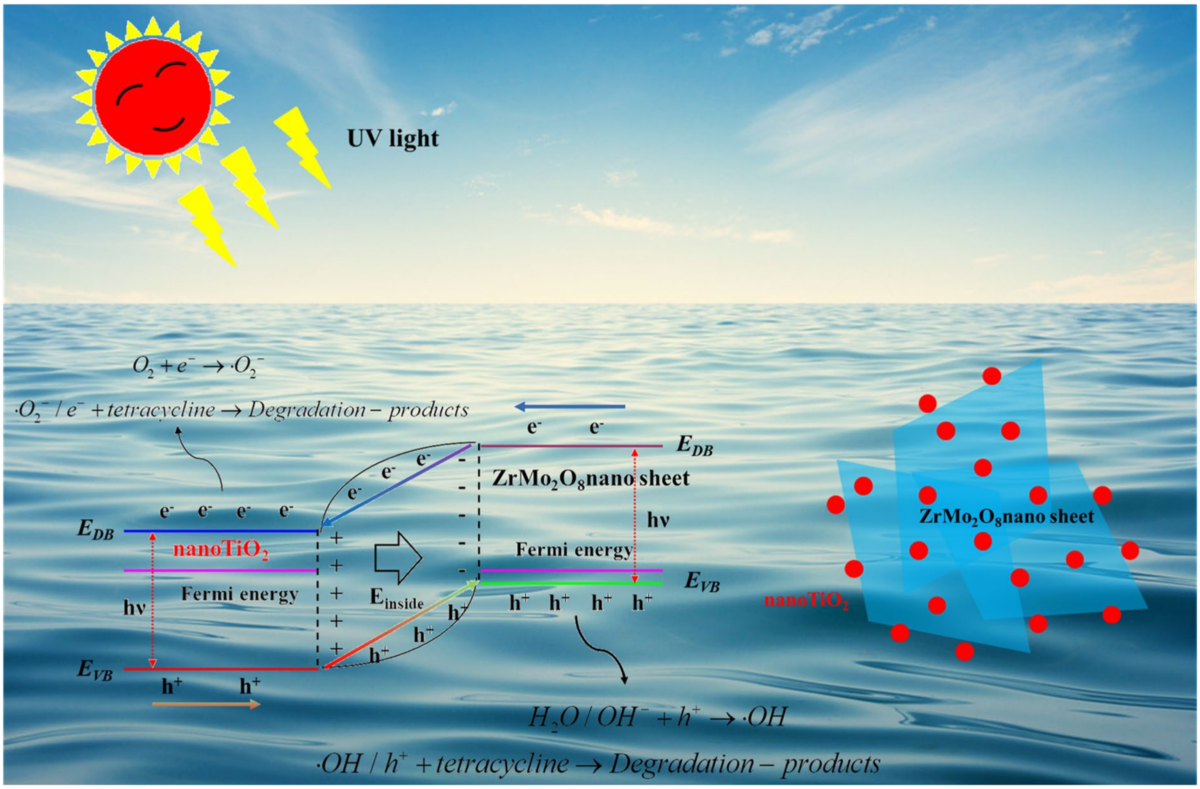

Fig. 17 Schematic diagram of the reaction mechanism

Funding This work is supported by the Zhenjiang City 2021 Key Research and Development Project (Social Development) under Grant No. SH2021020, the Science Foundation of Jiangsu Colleges and Universities (Grant Nos. 17KJD610001 and 17KJD610002), and the 2021 Jiangsu Province University Students Innovation and Entrepreneurship Training Program Project (202114000015Y).

Declarations

Conflict of interest The authors declare no competing interests.

References

1. Giannakis S, Lin K-YA, Ghanbari F (2021) A review of the recent advances on the treatment of industrial wastewaters by sulfate radical-based advanced oxidation processes (SR-AOPs). Chem Eng J 406:127083. https://doi.org/10.1016/j.cej.2020.127083
2. Deng D, Lamssali M, Aryal N, Ofori-Boadu A, Jha MK, Samuel RE (2020) Textiles wastewater treatment technology: a review. Water Environ Res 92:1805–1810. https://doi.org/10.1002/wer.1437
3. Han T, Zheng J, Han Y et al (2021) Comprehensive insights into core microbial assemblages in activated sludge exposed to textile-dyeing wastewater stress. Sci Total Environ 791:148145. https://doi.org/10.1016/j.scitotenv.2021.148145
4. da Silva GS, dos Santos FA, Roth G, Frankenberg CLC (2019) Electroplating for chromium removal from tannery wastewater. Int J Environ Sci Technol 17:607–614. https://doi.org/10.1007/s13762-019-02494-1
5. Sharma P, Tripathi S, Chandra R (2021) Metagenomic analysis for profiling of microbial communities and tolerance in metal-polluted pulp and paper industry wastewater. Bioresour Technol 324:124681. https://doi.org/10.1016/j.biortech.2021.124681
6. Isosaari P, Hermanowicz SW, Rubin Y (2010) Sustainable natural systems for treatment and disposal of food processing wastewater. Crit Rev Environ Sci Technol 40:662–697. https://doi.org/10.1080/10643380802359396
7. Ahmad UM, Pu Y, Qi W, Foster NR, Chen J-F, Wang D (2017) Efficient treatment of actual pharmaceutical wastewater by wet oxidation process in subcritical water apparatus. Can J Chem Eng 95:2056–2062. https://doi.org/10.1002/cjce.22885
8. Cheng D, Ngo HH, Guo W et al (2020) A critical review on antibiotics and hormones in swine wastewater: water pollution problems and control approaches. J Hazard

Mater 387:121682. https://doi.org/10.1016/j.jhazmat.2019.121682

9. Fu J, Zhang Q, Huang B, Fan N, Jin R (2020) A review on anammox process for the treatment of antibiotic-containing wastewater: linking effects with corresponding mechanisms. Front Environ Sci Eng 15:17. https://doi.org/10.1007/s11783-020-1309-y
10. Gholipour S, Mohammadi F, Nikaeen M et al (2021) COVID-19 infection risk from exposure to aerosols of wastewater treatment plants. Chemosphere 273:129701. https://doi.org/10.1016/j.chemosphere.2021.129701
11. Bogler A, Packman A, Furman A et al (2020) Rethinking wastewater risks and monitoring in light of the COVID-19 pandemic. Nat Sustain 3:981–990. https://doi.org/10.1038/s41893-020-00605-2
12. Zhu T-t, Su Z-x, Lai W-x, Zhang Y-b, Liu Y-w (2021) Insights into the fate and removal of antibiotics and antibiotic resistance genes using biological wastewater treatment technology. Sci Total Environ 776:145906. https://doi.org/10.1016/j.scitotenv.2021.145906
13. Li S, Yang Q, Ye Y (2017) Preparation of activated carbon from herbal residues and kinetics of cephalosporin antibiotic adsorption in wastewater. BioResources 12:2768–2779. https://doi.org/10.15376/biores.12.2.2768-2779
14. Michael-Kordatou I, Karaolia P, Fatta-Kassinos D (2018) The role of operating parameters and oxidative damage mechanisms of advanced chemical oxidation processes in the combat against antibiotic-resistant bacteria and resistance genes present in urban wastewater. Water Res 129:208–230. https://doi.org/10.1016/j.watres.2017.10.007
15. Lu H, Zou W, Chai P, Wang J, Bazinet L (2016) Feasibility of antibiotic and sulfate ions separation from wastewater using electrodialysis with ultrafiltration membrane. J Cleaner Prod 112:3097–3105. https://doi.org/10.1016/j.jclepro.2015.09.091
16. Hou J, Chen Z, Gao J et al (2019) Simultaneous removal of antibiotics and antibiotic resistance genes from pharmaceutical wastewater using the combinations of up-flow anaerobic sludge bed, anoxic-oxic tank, and advanced oxidation technologies. Water Res 159:511–520. https://doi.org/10.1016/j.watres.2019.05.034
17. Adeyemi JO, Ajiboye T, Onwudiwe DC (2021) Mineralization of antibiotics in wastewater via photocatalysis. Water Environ Res 232:219. https://doi.org/10.1007/s11270-021-05167-3
18. Sudhaik A, Raizada P, Shandilya P, Singh P (2018) Magnetically recoverable graphitic carbon nitride and $NiFe_2O_4$ based magnetic photocatalyst for degradation of oxytetracycline antibiotic in simulated wastewater under solar light. J Environ Chem Eng 6:3874–3883. https://doi.org/10.1016/j.jece.2018.05.039
19. Nguyen Le Minh T, Kim J, Bach Long G et al (2019) Ag-doped graphitic carbon nitride photocatalyst with remarkably enhanced photocatalytic activity towards antibiotic in hospital wastewater under solar light. J Ind Eng Chem 80:597–605. https://doi.org/10.1016/j.jiec.2019.08.037
20. Buzzetti L, Crisenza GEM, Melchiorre P (2019) Mechanistic studies in photocatalysis. Angew Chem Int Ed 58:3730–3747. https://doi.org/10.1002/anie.201809984
21. Chen C, Wang L, Cheng T et al (2022) $Ag_3PO_4/AgSbO_3$ composite as novel photocatalyst with significantly enhanced activity through a Z-scheme degradation mechanism. J Iran Chem Soc 19:821–838. https://doi.org/10.1007/s13738-021-02345-2
22. Wu S, Li X, Tian Y, Lin Y, Hu YH (2021) Excellent photocatalytic degradation of tetracycline over black anatase-TiO_2 under visible light. Chem Eng J 406:126747. https://doi.org/10.1016/j.cej.2020.126747
23. Kumar A, Sharma G, Naushad M et al (2020) Bio-inspired and biomaterials-based hybrid photocatalysts for environmental detoxification: a review. Chem Eng J 382:122937. https://doi.org/10.1016/j.cej.2019.122937
24. Atta-Eyison AA, Anukwah GD, Zugle R (2021) Photocatalysis using zinc oxide-zinc phthalocyanine composite for effective mineralization of organic pollutants. Catal Commun 160:106357. https://doi.org/10.1016/j.catcom.2021.106357
25. Zhao F, Liu Y, Ben Hammouda S et al (2020) MIL-101(Fe)/g-C_3N_4 for enhanced visible-light-driven photocatalysis toward simultaneous reduction of Cr(VI) and oxidation of bisphenol A in aqueous media. Appl Catal B 272:119033. https://doi.org/10.1016/j.apcatb.2020.119033
26. Cheung PL, Kapper SC, Zeng T, Thompson ME, Kubiak CP (2019) Improving photocatalysis for the reduction of CO_2 through non-covalent supramolecular assembly. J Am Chem Soc 141:14961–14965. https://doi.org/10.1021/jacs.9b07067
27. Lee H, Kim M, Lee H (2021) Reducing the photodegradation of perovskite quantum dots to enhance photocatalysis in CO_2 reduction. Catalysts 11:61. https://doi.org/10.3390/catal11010061
28. Ortiz Rabell G, Alfaro Cruz MR, Juarez-Ramirez I (2021) Hydrogen production of ZnO and ZnO/Ag films by photocatalysis and photoelectrocatalysis. Mater Sci Semicond Process 134:105985. https://doi.org/10.1016/j.mssp.2021.105985
29. Shangguan W, Kudo A, Jiang Z, Yamaguchi Y (2021) Photocatalysis: from solar light to hydrogen energy. Front Energy 15:565–567. https://doi.org/10.1007/s11708-021-0784-6
30. Kumar A, Sharma G, Kumari A et al (2021) Construction of dual Z-scheme g-$C_3N_4/Bi_4Ti_3O_{12}/Bi_4O_5I_2$ heterojunction for visible and solar powered coupled photocatalytic antibiotic degradation and hydrogen production: boosting via I^-/I_3^- and Bi^{3+}/Bi^{5+} redox mediators. Appl Catal B 284:119808. https://doi.org/10.1016/j.apcatb.2020.119808
31. Shi W, Li M, Huang X, Ren H, Yan C, Guo F (2020) Facile synthesis of 2D/2D $Co_3(PO_4)_2$/g-C_3N_4 heterojunction for highly photocatalytic overall water splitting under visible light. Chem Eng J 382:122960. https://doi.org/10.1016/j.cej.2019.122960
32. Pan M, Teng X, Li M et al (2021) A facile approach for surface modification of TiO_2 nanosheets to enhance photocatalytic hydrogen evolution activity. J Nanopart Res 23:260. https://doi.org/10.1007/s11051-021-05369-0
33. Meng A, Zhang L, Cheng B, Yu J (2019) Dual cocatalysts in TiO_2 photocatalysis. Adv Mater 31:1807660. https://doi.org/10.1002/adma.201807660

34. Liu W, Peng R, Pan J (2021) In situ synthesis of cubic PtPd bimetallic co-catalyst on C_3N_4 nanosheets for photocatalytic hydrogen generation. J Nanopart Res 23:17. https://doi.org/10.1007/s11051-020-05133-w
35. Sithole MP, Mafa PJ, de Kock LA, Viljoen E, Kuvarega AT (2021) Visible light active g-C_3N_4 sheets/CdS heterojunction photocatalyst for decolourisation of acid blue (AB-25). J Nanopart Res 23:16. https://doi.org/10.1007/s11051-020-05114-z
36. Shi W, Yang S, Sun H et al (2020) Carbon dots anchored high-crystalline g-C_3N_4 as a metal-free composite photocatalyst for boosted photocatalytic degradation of tetracycline under visible light. J Mater Sci 56:2226–2240. https://doi.org/10.1007/s10853-020-05436-2
37. Li F, Li Z, Cai Y, Zhang M, Shen Y, Wang W (2017) Afterglow photocatalysis of Ag_3PO_4 through different afterglow coatings and photocatalysis mechanism. Mater Lett 208:111–114. https://doi.org/10.1016/j.matlet.2017.04.106
38. Luo L, Li Y, Hou J, Yang Y (2014) Visible photocatalysis and photostability of Ag_3PO_4 photocatalyst. Appl Surf Sci 319:332–338. https://doi.org/10.1016/j.apsusc.2014.04.154
39. Shi W, Liu C, Li M, Lin X, Guo F, Shi J (2020) Fabrication of ternary $Ag_3PO_4/Co_3(PO_4)_2$/g-C_3N_4 heterostructure with following type II and Z-scheme dual pathways for enhanced visible-light photocatalytic activity. J Hazard Mater 389:121907. https://doi.org/10.1016/j.jhazmat.2019.121907
40. Pan L, Muhammad T, Ma L et al (2016) MOF-derived C-doped ZnO prepared via a two-step calcination for efficient photocatalysis. Appl Catal B 189:181–191. https://doi.org/10.1016/j.apcatb.2016.02.066
41. Samadi M, Zirak M, Naseri A, Khorashadizade E, Moshfegh AZ (2016) Recent progress on doped ZnO nanostructures for visible-light photocatalysis. Thin Solid Films 605:2–19. https://doi.org/10.1016/j.tsf.2015.12.064
42. Carbuloni CF, Savoia JE, Santos JSP et al (2020) Degradation of metformin in water by TiO_2-ZrO_2 photocatalysis. J Environ Manage 262:110347. https://doi.org/10.1016/j.jenvman.2020.110347
43. Renuka L, Anantharaju KS, Sharma SC et al (2016) Hollow microspheres Mg-doped ZrO_2 nanoparticles: green assisted synthesis and applications in photocatalysis and photoluminescence. J Alloys Compd 672:609–622. https://doi.org/10.1016/j.jallcom.2016.02.124
44. Wang X, Xiong W, Li X et al (2018) Fabrication of MoS_2@g-C_3N_4 core-shell nanospheres for visible light photocatalytic degradation of toluene. J Nanopart Res 20:243. https://doi.org/10.1007/s11051-018-4340-1
45. Peng Y, Li J, Qian X, Zhang J, Lin J (2018) Photodeposition of ultrathin MoS_2 nanosheets onto cubic CdS for efficient photocatalytic H_2 evolution. J Nanopart Res 20:104. https://doi.org/10.1007/s11051-018-4211-9
46. Guo F, Huang X, Chen Z et al (2021) Construction of Cu3P-ZnSnO3-g-C3N4 p-n-n heterojunction with multiple built-in electric fields for effectively boosting visible-light photocatalytic degradation of broad-spectrum antibiotics. Sep Purif Technol 265:118477. https://doi.org/10.1016/j.seppur.2021.118477
47. Mancheva MN, Iordanova RS, Dimitriev YB, Tyuliev GG, Iliev TC (2011) Influence of heat treatment on the phase transition of ZrMo2O8 and photocatalytic activity. Cent Eur J Chem 9:460–465. https://doi.org/10.2478/s11532-011-0027-5
48. Sahoo PP, Sumithra S, Madras G, Row TNG (2009) Synthesis, characterization, and photocatalytic properties of ZrMo2O8. J Phys Chem C 113:10661–10666. https://doi.org/10.1021/jp901897s
49. Sahoo PP, Sumithra S, Madras G, Row TNG (2009) Synthesis, structure and photocatalytic properties of beta-$ZrMo_2O_8$. Bull Mater Sci 32:337–342. https://doi.org/10.1007/s12034-009-0048-2
50. Liu C, Qin Y, Guo W et al (2022) Visible-light-driven photocatalysis over nano-TiO_2 with different morphologies: from morphology through active site to photocatalytic performance. Appl Surf Sci 580:152262. https://doi.org/10.1016/j.apsusc.2021.152262
51. Lin Z, Shen W, Corriou J-P, Chen X, Xi H (2022) Assessment of multiple environmental factors on the adsorptive and photocatalytic removal of gaseous formaldehyde by a nano-TiO_2 colloid: experimental and simulation studies. J Colloid Interface Sci 608:1769–1781. https://doi.org/10.1016/j.jcis.2021.10.095
52. Moradi M, Hasanvandian F, Isari AA, Hayati F, Kakavandi B, Setayesh SR (2021) CuO and ZnO co-anchored on g-C_3N_4 nanosheets as an affordable double Z-scheme nanocomposite for photocatalytic decontamination of amoxicillin. Appl Catal B 285:119838. https://doi.org/10.1016/j.apcatb.2020.119838
53. Liang ZQ, Xue YJ, Wang XY et al (2021) Co doped MoS_2 as cocatalyst considerably improved photocatalytic hydrogen evolution of g-C_3N_4 in an alkalescent environment. Chem Eng J 421:130016. https://doi.org/10.1016/j.cej.2021.130016
54. Low JX, Yu JG, Jaroniec M, Wageh S, Al-Ghamdi AA (2017) Heterojunction photocatalysts. Adv Mater 29:1601694. https://doi.org/10.1002/adma.201601694
55. You JH, Bao WT, Wang L, Yan AG, Guo R (2021) Preparation, visible light-driven photocatalytic activity, and mechanism of multiphase CdS/C_3N_4 inorganic-organic hybrid heterojunction. J Alloys Compd 866:158921. https://doi.org/10.1016/j.jallcom.2021.158921
56. Su Q, Zhu LL, Zhang MR et al (2021) Construction of a bioinspired hierarchical $BiVO_4$/BiOCl heterojunction and its enhanced photocatalytic activity for phenol degradation. ACS Appl Mater Interfaces 13:32906–32915. https://doi.org/10.1021/acsami.1c05117
57. Zhang C, Wang L, Yuan F et al (2020) Construction of p-n type $Ag_3PO_4/CdWO_4$ heterojunction photocatalyst for visible-light-induced dye degradation. Appl Surf Sci 534:147544. https://doi.org/10.1016/j.apsusc.2020.147544
58. Li Y, Fu M, Wang R, Wu S, Tan X (2022) Efficient removal TC by Zn@SnO_2/PI via the synergy of adsorption and photocatalysis under visible light. Chem Eng J 444:136567. https://doi.org/10.1016/j.cej.2022.136567
59. Xue Y, Tang W, Gu H et al (2022) Flexible Bi_2MoO_6/N-doped carbon nanofiber membrane enables tetracycline photocatalysis for environmentally safe

growth of Vigna radiata. J Alloys Compd 902:163860. https://doi.org/10.1016/j.jallcom.2022.163860

60. Kresse F (1996) Efficient iterative schemes for ab initio total-energy calculations using a plane-wave basis set. Phys Rev B: Condens Matter Mater Phys 54:11169–11186. https://doi.org/10.1103/PhysRevB.54.11169
61. Hohenberg P, Kohn W (1964) InhomogeIIeous electron gas. Phys Rev 136:B864–B871. https://doi.org/10.1103/PhysRev.136.B864
62. Kohn W, Sham L (1965) Self-consistent equations including exchange and correlation effects. Phys Rev 140:A1133–A1138. https://doi.org/10.1103/physrev.140.a1133
63. Perdew JP, Chevary JA, Vosko SH et al (1992) Atoms, molecules, solids, and surfaces: applications of the generalized gradient approximation for exchange and correlation. Phys Rev B: Condens Matter Mater Phys 46:6671–6687. https://doi.org/10.1103/PhysRevB.46.6671
64. Perdew JP, Burke K, Ernzerhof M (1996) Generalized gradient approximation made simple. Phys Rev Lett 77:3865–3868. https://doi.org/10.1103/PhysRevLett.77.3865
65. Ghosh S, Samanta M, Sen D, Sarkar S, Sarkar S, Chattopadhyay KK (2021) Photocatalytic and sonocatalytic dye degradation by sulfur vacancy rich ZnS nanopowder. J Nanopart Res 23:160. https://doi.org/10.1007/s11051-021-05283-5
66. Idris AO, Mafa PJ, Oseghe EO, Msagati TAM, Feleni U, Mamba BB (2021) A facile approach for the preparation of NiONPs@MnO_2NRs nanocomposite material and its photocatalytic activity. J Nanopart Res 23:142. https://doi.org/10.1007/s11051-021-05257-7
67. Liu CB, Wang LL, Tang YH et al (2015) Vertical single or few-layer MoS_2 nanosheets rooting into TiO_2 nanofibers for highly efficient photocatalytic hydrogen evolution. Appl Catal B 164:1–9. https://doi.org/10.1016/j.apcatb.2014.08.046
68. Basahel SN, Ali TT, Mokhtar M, Narasimharao K (2015) Influence of crystal structure of nanosized ZrO_2 on photocatalytic degradation of methyl orange. Nanoscale Res Lett 10:73. https://doi.org/10.1186/s11671-015-0780-z
69. Huang J, Dou L, Li J, Zhong J, Li M, Wang T (2021) Excellent visible light responsive photocatalytic behavior of N-doped TiO_2 toward decontamination of organic pollutants. J Hazard Mater 403:123857. https://doi.org/10.1016/j.jhazmat.2020.123857
70. Kumar A, Sharma SK, Sharma G et al (2021) Silicate glass matrix@$Cu_2O/Cu_2V_2O_7$ p-n heterojunction for enhanced visible light photo-degradation of sulfamethoxazole: high charge separation and interfacial transfer. J Hazard Mater 402:123790. https://doi.org/10.1016/j.jhazmat.2020.123790
71. Shi W, Shu K, Sun H et al (2020) Dual enhancement of capturing photogenerated electrons by loading CoP nanoparticles on N-deficient graphitic carbon nitride for efficient photocatalytic degradation of tetracycline under visible light. Sep Purif Technol 246:116930. https://doi.org/10.1016/j.seppur.2020.116930
72. Chen C, Wang L, Cheng T, Zhang X, Tian Y, Shi Y (2021) Sliver doped sodium antimonate with greatly reduced the band gap for efficiently enhanced photocatalytic activities under visible light (experiment and DFT calculation). Mater Res-Ibero-Am J 24:e20210100. https://doi.org/10.1590/1980-5373-mr-2021-0100